DEVELOPMENT OF FLUORESCENCE LIFETIME IMAGING MICROSCOPY TECHNIQUES FOR ANALYSIS OF SINGLE EXTRACELLULAR VESICLES

BY

JANET ELISE SORRELLS

THESIS

Submitted in partial fulfillment of the requirements
for the degree of Master of Science in Bioengineering
in the Graduate College of the
University of Illinois at Urbana-Champaign, 2020

Urbana, Illinois

Adviser:

Professor Stephen A. Boppart

ABSTRACT

Extracellular vesicles (EVs) make up a variety of μm and sub-μm phospholipid membrane-bound particles released by cells. EVs have recently become an intense topic of interest as more is learned about their many purposes, such as their function in cell-to-cell communication in diseases such as cancer. EVs are extremely heterogeneous by nature, effecting the need for single EV characterization techniques. Moreover, studies often lack the ability to measure functional properties of EVs, focusing mostly on size, concentration, and biochemical makeup. This thesis presents the first use of two-photon fluorescence lifetime imaging microscopy (FLIM) to characterize the free and protein-bound reduced forms of nicotinamide adenine dinucleotide and nicotinamide adenine dinucleotide phosphate (NAD(P)H) content of EVs derived from cells, human urine, and human serum with single EV resolution. The fluorescence lifetimes of NAD(P)H in EVs isolated from an aggressive human breast cancer cell line follow a wide Gaussian distribution, indicating the presence of a range of protein-bound and free NAD(P)H. Changes in the metabolic conditions of parent cells were reflected in the mean NAD(P)H fluorescence lifetime of the EVs they produced, and the functional aspects of stored and fresh EVs were evaluated, showing that storage may change the NAD(P)H fluorescence lifetime signature of EVs. Functional characterization was explored by imaging the response of macrophages to EVs. When compared to that of live cells, the fluorescence lifetime distribution of NAD(P)H in EVs was most similar to the cytosol out of the examined cellular components, consistent with previous proteomic studies. Compared to cytosol, EVs had a larger protein-bound NAD(P)H fluorescence lifetime component, likely due to protein and metabolite enrichment of EVs, which has also been seen in proteomic studies. This suggests that FLIM of NAD(P)H in EVs could be a valuable tool for characterization of EV subpopulations and should be explored for additional studies.

ACKNOWLEDGMENTS

I would like to thank my advisor Professor Stephen Boppart for his unconditional support and for always inspiring me with new ideas. I would also like to thank him for the opportunity to work with all of the wonderful people I have met in the Biophononics Imaging Laboratory (BIL) here at the University of Illinois at Urbana-Champaign.

I also am thankful to past and present BIL members for their continuous support and encouragement. I would specifically like to thank Dr. Marina Marjanovic, Dr. Prabuddha Mukherjee, Dr. Edita Aksamitiene, Dr. Aneesh Alex, Eric Chaney, and Darold Spillman for advice, technical assistance, and always being willing to teach me new things. I am also grateful to Rishee Iyer and Lilian Yang for their friendship and support.

Finally, I would like to thank my family and friends for sticking with me through the highs and lows of life outside of BIL.

TABLE OF CONTENTS

1. Introduction and background……1
1.1. Overview……1
1.2. Cancer and EV biology……2
1.3. Optical biochemical characterization of EVs……9
1.4. Two-photon fluorescence lifetime imaging microscopy……12
2. Experimental methods for imaging NAD(P)H in extracellular vesicles……25
2.1. Motivation: label-free single EV analysis……25
2.2. Cell culture and EV isolation……25
2.3. EV sample characterization……27
2.4. Embedding and imaging……28
2.5. Image segmentation with blob detection algorithm……30
2.6. Lifetime analysis of single EVs……32
2.7. Discussion……35
3. NAD(P)H fluorescence lifetime of extracellular vesicles...……37
3.1. Motivation: understanding EV NAD(P)H fluorescence lifetime……37
3.2. Heterogeneity of EV fluorescence lifetimes……37
3.3. Negative control……38
3.4. Repeatability……39
3.5. Human biofluid-derived EVs……40
3.6. Discussion……42
4. Functional characterization of extracellular vesicles……44
4.1. Motivation: functional analysis of EVs……44
4.2. Storage of EVs……45
4.3. Effect of EVs on macrophages……47
4.4. Discussion……50
5. Relationship between extracellular vesicles and parent cells……51
5.1. Motivation: EVs as biomarkers of disease……51
5.2. Metabolic perturbations of cells……51
5.3. EVs and spatial analysis of cells……52
5.4. Discussion……54
6. Conclusions and future work……60
6.1. Conclusions……60
6.2. Current challenges in nonlinear optical imaging of EVs……61
6.3. Future directions……62
7. References……64

1. INTRODUCTION AND BACKGROUND

1.1. Overview

In the US, over 1.7 million new cases of cancer and over 600,000 cancer deaths were reported in 2019 [1]. Of those, female breast cancer had the highest incidence, or was the most commonly reported as new cases of cancer, affecting an estimated 268,600 women, and the second most common cause of cancer death, killing an estimated 41,760 women [1]. Breast cancer rates in the US are steady overall, but are increasing for women of lower socioeconomic status, specifically for Black women and Asian and Pacific Islander women [2]. Breast cancer survival is highly dependent on access to early detection and affordable care, both of which can significantly decrease mortality, though even the best care cannot guarantee survival [3,4]. The World Health Organization (WHO) has declared that the two main factors needed for early detection of cancer are early diagnosis, "the recognition of symptomatic cancer in patients," and screening, "the identification of asymptomatic disease in apparently healthy target populations" [3].

Recent studies indicate that one potential candidate for these early detection mechanisms is the characterization of extracellular vesicles (EVs) [5]. EVs are membrane-bound particles, around 50 to 2000 nm in diameter, released by cells and used in cell-to-cell communication. They are present in both healthy conditions and in the diseased state, and notably are involved in cancer and metastasis [6]. The EV field has recently broadly expanded with new methods of EV isolation and characterization in order to better examine their potential for use as biomarkers of disease, such as for cancer early detection, and also to improve our understanding of fundamental EV biology and their role in processes such as disease spread and metastasis [5]. However, the lack of ability to reliably characterize the heterogeneity of EV composition provides a barrier to EV research, and better tools for EV analysis need to be developed [7,8]. Recent work has shown that

nonlinear optical autofluorescence imaging can be used to image and characterize EVs both *in vivo* and *in vitro* [9]. This previous work focused on characterizing vesicles rich in reduced nicotinamide adenine dinucleotide (NADH) and reduced nicotinamide adenine dinucleotide phosphate (NADPH), together termed NAD(P)H. NAD(P)H was found to have increased autofluorescence in cancer-associated EVs [9].

This thesis details the first use of fluorescence lifetime imaging microscopy (FLIM) to better characterize the NAD(P)H content of EVs. Compared to autofluorescence intensity imaging, FLIM provides more information about the nanoscale environment of the fluorophore such as changes in pH, temperature, and protein interactions [10]. FLIM is rooted in the principle that the probability density function of fluorescence photon emission vs. time follows an exponential decay, characteristic of the fluorophore and its environment. On a larger scale this translates to an exponential decay of intensity vs. time that can be measured and characterized [10]. FLIM of NAD(P)H has been widely used in cells and tissues to provide functional information about metabolism, relying on characteristic shifts in the fluorescence lifetime of NAD(P)H due to protein interactions in glycolysis, the tricarboxylic acid (TCA) cycle, and the electron transport chain (ETC) [11]. Developing novel EV analysis methods with techniques like FLIM can both improve our collective understanding of EVs and also advance towards the possibility of EV-based diagnostics.

1.2. Cancer and EV biology

1.2.1. Cellular energy metabolism

Each cell contains a large variety of proteins used to break down larger molecules into smaller ones in catabolic pathways to create and store energy. This energy is essential for all cellular functions, and the byproducts of catabolism can also be used as building blocks to create

the necessary proteins, lipids, nucleic acids, and other biomolecules to sustain life. The primary fuel used for cellular metabolism is glucose, a six-carbon sugar, which is used to produce the primary energy storage molecule: adenosine triphosphate (ATP). Generally, in a catabolic pathway, adenosine diphosphate (ADP) and inorganic phosphate (P_i) are combined using released energy from the glucose breakdown process to create ATP. This ATP can then be broken back down into ADP and P_i to provide energy for cellular work or macromolecule synthesis. The first step in glucose breakdown is glycolysis, a process by which glucose is broken down into two three-carbon molecules of pyruvate that uses two molecules of ATP but phosphorylates four total molecules of ADP, for a net energy gain of two ATPs. During one step of the glycolysis process, the essential cofactor nicotinamide adenine dinucleotide (NAD+) acts as an electron acceptor to become reduce nicotinamide adenine dinucleotide (NADH) [12]. A simplified glycolysis pathway is shown in **Figure 1.1**.

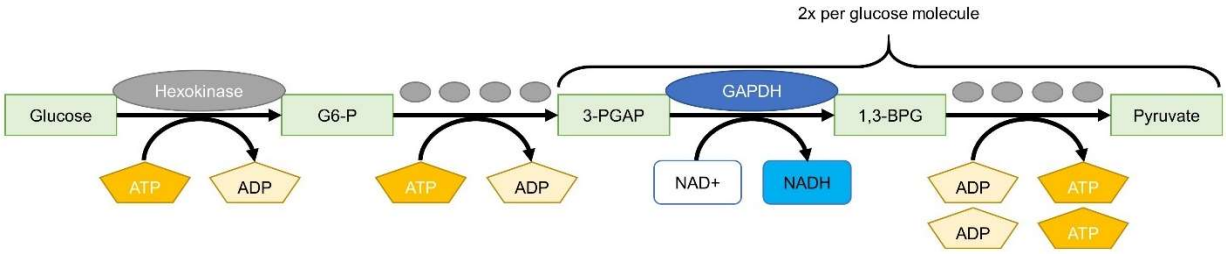

Figure 1.1: Schematic presentation of glycolysis. Glucose, a six-carbon sugar, is broken down into two molecules of pyruvate, a three-carbon sugar, and in the process converts two net molecules of ADP to ATP. An electron pair from each 3-PGAP molecule is taken by an NAD+ molecule, forming NADH.

After glycolysis, under normal cellular conditions, pyruvate is primarily sent into the mitochondria where the TCA cycle and ETC occur for further degradation and efficient ATP production. **Figure 1.2** shows the two main fates of pyruvate: conversation into lactate or entering the mitochondria for conversion into acetyl CoA for the TCA cycle. Acetyl CoA, a 2-carbon molecule, enters the TCA cycle to combine with a 4-carbon molecule, oxaloacetate (OAA),

forming a 6-carbon molecule. Through a series of reactions, two CO_2 molecules are released and three more NAD+ molecules are converted into NADH, and OAA is recovered, able to bind with acetyl CoA and begin the cycle again. The ETC uses the reduced cofactors NADH and reduced flavin adenine dinucleotide ($FADH_2$), pumping their H+ ions across the inner mitochondrial membrane, and transporting their electrons to be accepted by O_2 to facilitate the creation of H_2O. These reactions cannot take place without the presence of oxygen in mitochondrial, resulting in it being termed "aerobic metabolism," as opposed to glycolysis, which does not require oxygen, and is termed "anaerobic." As a result of the aerobic processes, ATP synthase uses the chemiosmotic gradient to phosphorylate ADP into ATP, generating up to 34 ATP per each molecule of glucose [12].

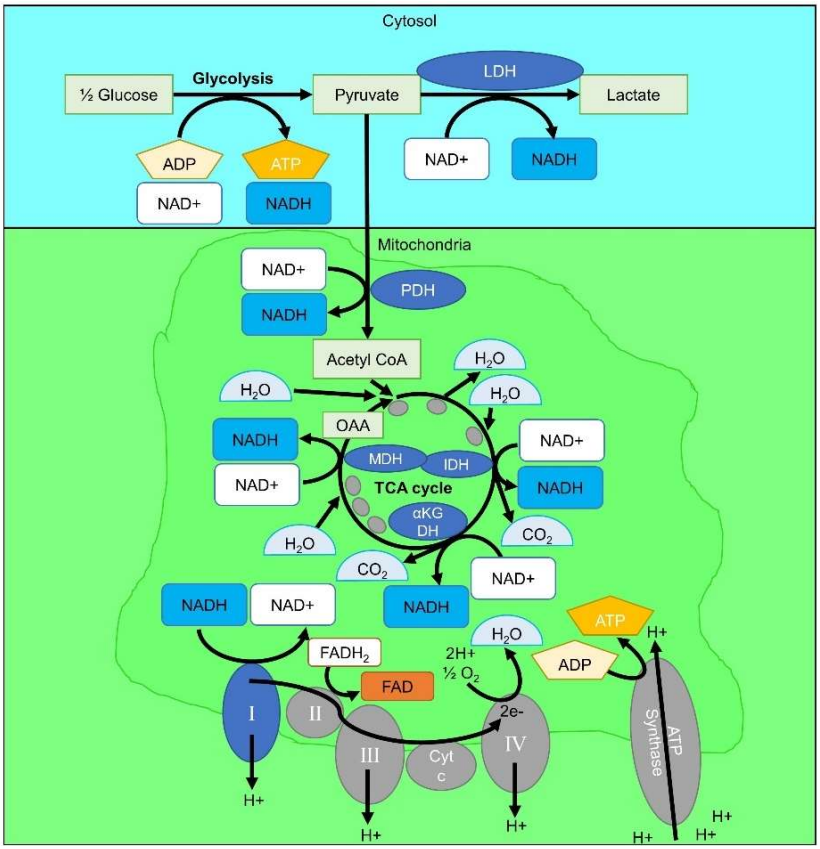

Figure 1.2: Cellular energy metabolism of glucose. Glucose is broken down into pyruvate via glycolysis, which can then enter the mitochondria to fuel the tricarboxylic acid (TCA) cycle and electron transport chain (ETC) for aerobic respiration. Without the presence of oxygen and/or in some diseased states, pyruvate is converted to lactate by lactate dehydrogenase (LDH).

However, the production of ATP is not the only possible fate of glucose in the cell. As shown in **Figure 1.3**, the glucose derivative glucse-6-phosphate (G6-P) can also be shifted towards the pentose phosphate pathway (PPP). The PPP occurs in the cytosol and generates reduced nicotinamide adenine dinucleotide phosphate (NADPH), which is essential for the antioxidant response, and creates intermediate molecules used in other biosynthetic pathways involved in nucleotide and amino acid synthesis. In addition, the PPP can result in creation of some of the same intermediates as glycolysis, so the relative need of a cell for NADH and NADPH is balanced by regulation of the fate of G6-P [12]. These metabolic pathways provide a non-exhaustive summary of cellular energy metabolism and the involvement of key cofactors such as NADH, NADPH, and FAD that accept and donate electrons throughout cytosolic and mitochondrial processes.

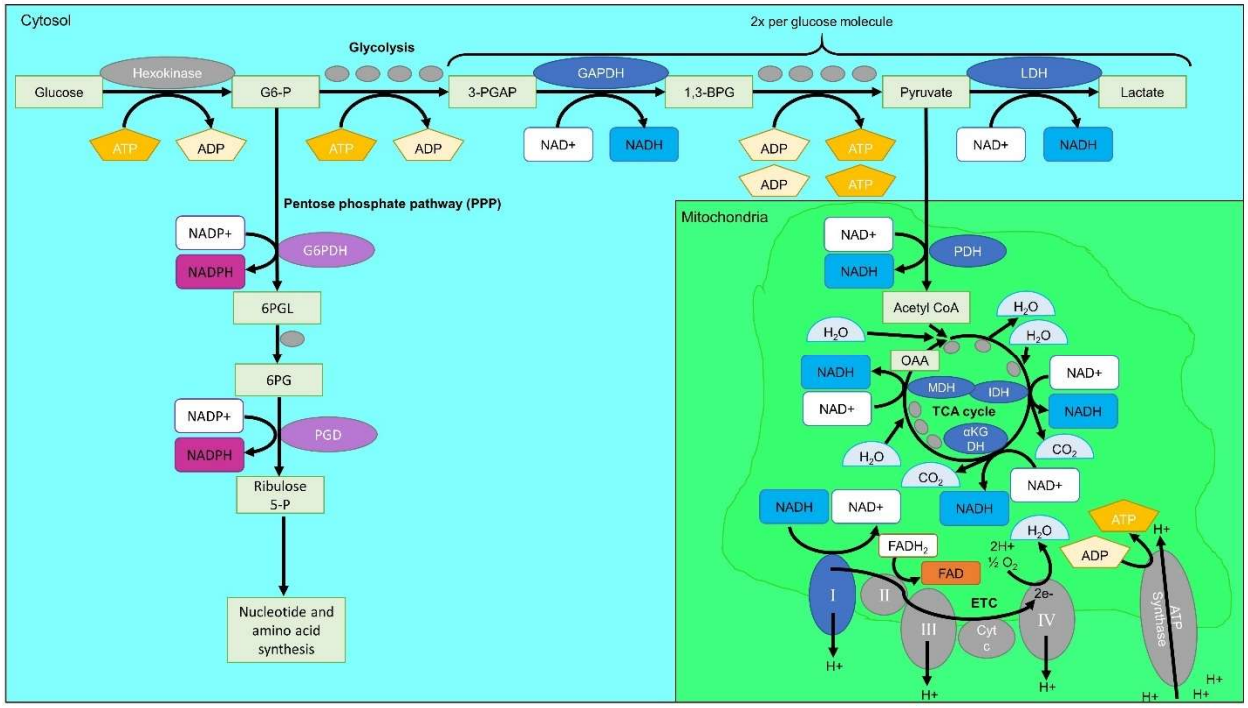

Figure 1.3: Key cellular fates glucose. Glucose can be split through glycolysis or can be shifted to the pentose phosphate pathway (PPP) to be used as building blocks for anabolic pathways and replenish the NADPH in the cell.

1.2.2. Tumor metabolism and metastasis

Cellular metabolism and the tumor microenvironment are highly linked; in fact, reprogramming of energy metabolism is classified as an emerging hallmark of cancer [13]. Normal cells convert glucose to pyruvate through glycolysis, then primarily send pyruvate to the mitochondria for participation in the TCA cycle and ETC, as detailed above in **Figure 1.2**. However, Otto Warburg discovered that cancer cell metabolism differs, often with downregulation of pyruvate-related metabolism in the mitochondria, and instead upregulating pyruvate conversion to lactate by lactate dehydrogenase (LDH) [13]. This metabolic shift toward glycolysis and away from mitochondrial metabolism occurs even in the presence of oxygen, and has thus been termed "aerobic glycolysis". This may seem counter-intuitive, since glycolysis, creating 2 ATP per glucose, is much less efficient in producing ATP than mitochondrial metabolism, which creates up to 34 ATP per glucose [13]. However, aerobic glycolysis provides multiple other benefits to cancer cells. This increased glucose uptake and lactate production facilitates increased tumor growth, decreased immune response, and nutrient deprivation of neighboring healthy, non-tumorous cells [13,14], as shown in **Figure 1.4**. This leads to local tumor cell proliferation and tumorigenesis.

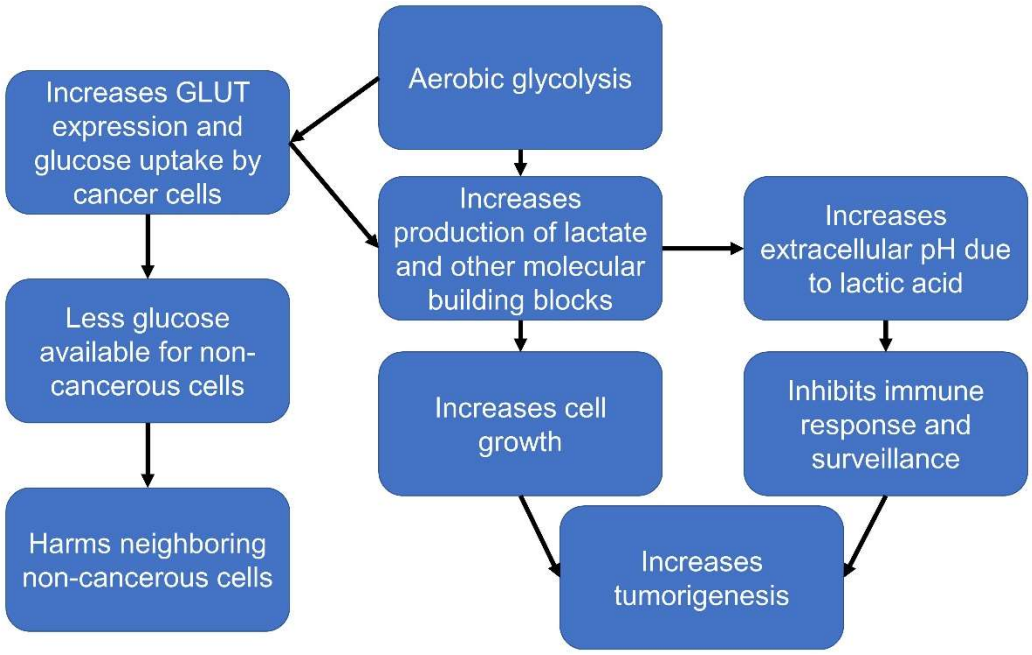

Figure 1.4: Aerobic glycolysis and its role in the tumor microenvironment. Aerobic glycolysis results in increased glucose uptake of cancer cells, which starves nearby non-cancerous cells, enabling the cancer to spread. Furthermore, increased molecule build block production is achieved through increased pentose phosphate pathway (PPP) activity and lactate production, which allows the cancer cells to grow and replicate more. The increased lactate and lactic acid also create a more acidic tumor microenvironment, which inhibits the immune response from subduing the cancer cells. All of this promotes tumorigenesis.

In addition to the ability to proliferate locally, malignant cancer is also characterized by its ability to spread to other areas of the body, in a process called metastasis. It is estimated that about 90% of all cancer deaths are due to metastases [15]. The process of cancer cells colonizing and forming metastases at additional locations throughout the body is not yet fully understood, though it is widely accepted that primary tumors release circulating tumor cells (CTCs) into the bloodstream that extravasate, stay dormant for some amount of time, and then eventually form secondary tumors [15]. The factors that lead to active secondary tumor formation are unclear, although the formation of a pre-metastatic niche prior to CTC arrival is thought to promote secondary tumor formation and decrease CTC dormancy period [15]. Recent work has identified EVs as key mediators of this pre-metastatic niche and promotion of CTC adaptation and activation in the pre-metastatic niche [6].

1.2.3. Extracellular vesicles

EVs are cell-derived membrane-bound particles, ranging from 50 to 2000 nm in diameter, that contain a variety of biomolecules, such as proteins, lipids, metabolites, and nucleic acids [6,16-19]. Recently, EVs have become a topic of intense investigation due to their wide variety of functions in cell-to-cell communication, their potential as biomarkers of disease, and their application in therapeutics [16,17,20-22].

EVs are known to function in systemic cell-to-cell communication, including metastasis; their plasma membrane allows them to safely carry contents between organs through bodily fluids such as blood or lymph [6]. EVs can contain different mRNA, miRNA, and other molecules that have the ability to alter and "reprogram" target cells, which can help to prepare the pre-metastatic niche to welcome CTCs [6]. Of special interest is miRNA, which alters gene expression through cytosolic mRNA silencing. Certain miRNAs have been found to be upregulated in EVs in cancer and other diseases [6,23].

With growing interest in EVs, there is an increased need to develop new methods of characterization [16-19], specifically with single EV resolution [8]. The morphology and size distribution of EVs are commonly characterized using dynamic light scattering (DLS) [24], nanoparticle tracking analysis (NTA) [25], electron microscopy [20,26], and atomic force microscopy (AFM) [27], all of which lack biochemical specificity. Characterization of EV molecular and biochemical content has been achieved using techniques such as Raman spectroscopy [28-30], Western blot [31], mass spectrometry [32,33], and nucleic acid sequencing [34]. While these techniques can provide a broad biochemical profile of bulk EV populations, they lack the ability to analyze characteristics of individual EVs and thus also lack the ability to quantify and assess the biochemical heterogeneity of EVs within a sample.

1.3. Optical biochemical characterization of EVs

Light scattering techniques such as DLS and NTA only report on the size and concentration of scatterers, whereas the aforementioned biochemically-sensitive techniques require such a large volume of EVs that they cannot report on EV heterogeneity. Fortunately, recent work has developed optical techniques with single EV resolution that can report on biochemical makeup.

1.3.1. Raman spectroscopy and flow cytometry

Raman spectroscopy, which probes the vibrational state of chemical bonds, has been used in conjunction with optical tweezers for single particle/EV trapping and characterization [35]. Synchronous Rayleigh and Raman scattering has been demonstrated for simultaneous chemical and size characterization of EVs, and showed that EVs from different origins had distinct spectral differences [28]. Recent advancements in flow cytometry allowing imaging of smaller (<500 nm) particles has been applied to single EV characterization [36]; however, flow cytometry requires fluorescence or magnetic bead tagging which is time-consuming and primarily targets surface proteins. Fluorescence tagging of EVs is further limited by the lack of universally accepted EV-specific proteins. The validation and specificity of fluorescence tags also causes uncertainty in flow cytometry data [16]. While Raman spectroscopy and flow cytometry both report on the biochemical makeup of the EVs, they do not provide information on intrinsic activity, functionality, or spatial distribution, all of which are critical parameters for EV analysis [16,18].

1.3.2. Nonlinear optical microscopy of EVs

Recent work has aimed to accomplish single EV functional and biochemical characterization with nonlinear optical microscopy, which achieves high spatial resolution (<500 nm), wide field-of-view imaging for correlating the spatial distribution of EVs to their tissue microenvironment, biochemical specificity, and functional reduction-oxidation ratio, or

optical redox ratio (ORR), information of single EVs [9,37,38]. This has been done using simultaneous label-free autofluorescence multiharmonic (SLAM) microscopy [9,37,39] and a combination of autofluorescence microscopy and coherent anti-Stokes Raman scattering (CARS) microscopy [38]. Characterization of EVs using autofluorescence microcopy has focused on examining the relative autofluorescence intensity of three essential metabolic cofactors: NADH, NADPH, and FAD [9,37,38].

As discussed previously (**Section 1.2.1**), NADH is a key cofactor in glycolysis, the TCA cycle, and the ETC, while the phosphorylated form of NADH, NADPH, plays a central role in biosynthetic pathways and antioxidant defense mechanisms. Collectively, the autofluorescence of NADH and NADPH is combined and referred to as "NAD(P)H" since their excitation and emission spectra are almost identical and impractical to distinguish [40]. Along with NADH, FAD is also an essential cofactor for the ETC and oxidative phosphorylation processes in the mitochondria. The relative autofluorescence intensities of NAD(P)H and FAD, ORR (calculations discussed in **Section 1.4.4**), is often used to estimate the ratio of NAD+ to NADH, which will increase as more NADH is oxidized to NAD+ at complex I in the mitochondrial ETC (**Figure 1.2**). Thus the ORR is used to characterize and quantify the metabolism of cells and tissues [41,42]. By extrapolating these functional measures to EVs, single EV metabolic characterization has been achieved. The NAD(P)H autofluorescence specifically has drawn interest since a higher NAD(P)H autofluorescence intensity was found to be associated with cancerous EVs both *in vivo* and in isolated EV samples [9,37,38]. **Figure 1.5** shows the increased relative autofluorescence of NAD(P)H in later stages of breast cancer, both in tissue and in EVs [9]. This finding warrants additional investigation of the NAD(P)H content of EVs and its potential as a biomarker for disease and may be a key to better understanding EV function and biogenesis.

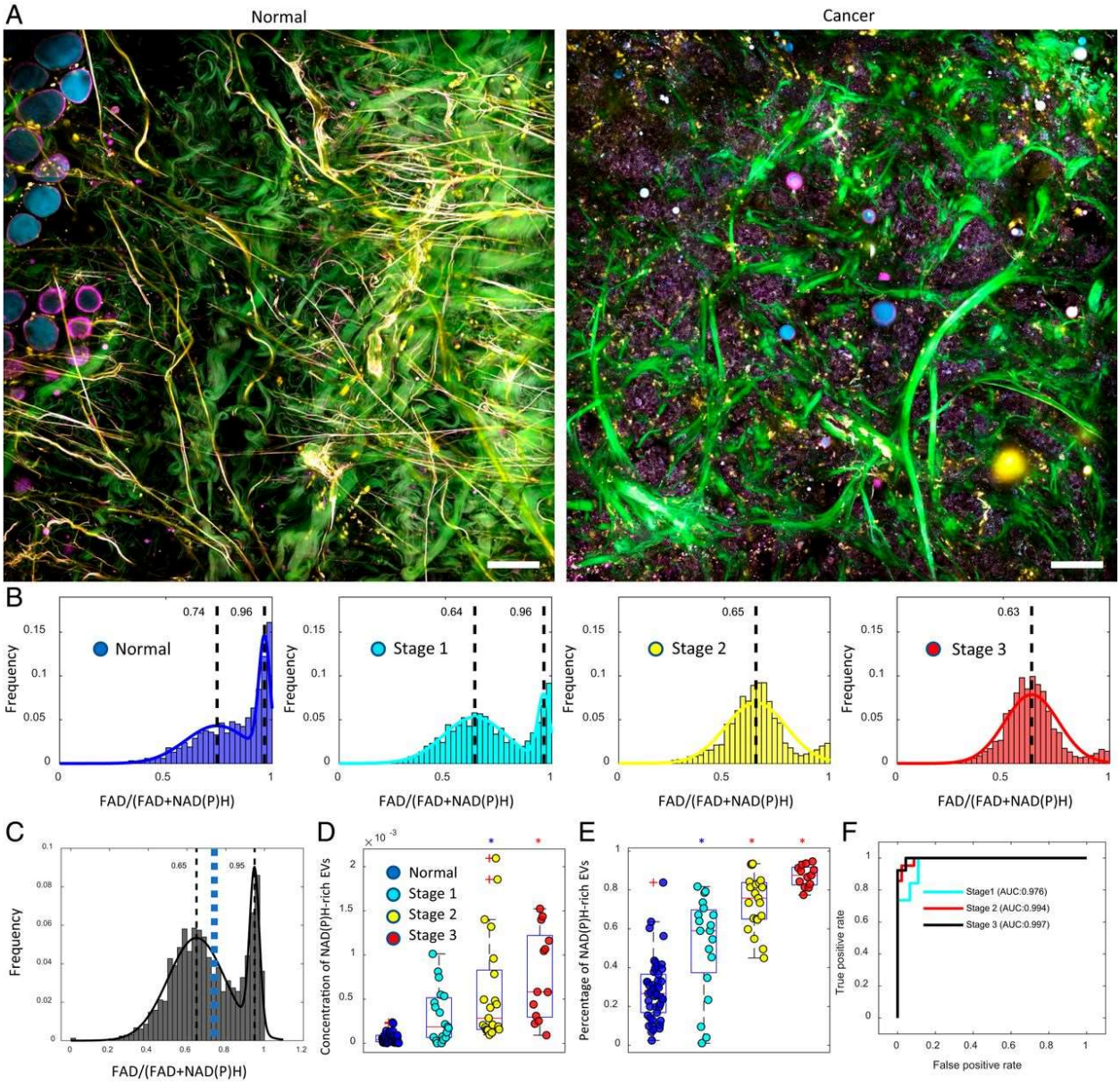

Figure 1.5: Correlation of optical redox ratio (ORR) in extracellular vesicles (EVs) with different stages of breast cancer [9]. (A) Simultaneous label-free autofluorescence multiharmonic (SLAM) microscopy images of fresh normal and cancerous tissue. Images are four channels co-registered: two-photon autofluorescence of FAD (*yellow*), three-photon autofluorescence of NAD(P)H (*cyan*), second harmonic generation (SHG) of collagen (*green*), and third harmonic generation (THG) of refractive index changes (*magenta*). Scale bars represent 100 μm. (B) Histograms of the number of EVs in breast tissue at the indicated stage of cancer by ORR (FAD/(FAD+NAD(P)H)) level. (C) Combined histogram of all EVs from normal and cancerous tissue. (D) Concentration and (E) percentage of NAD(P)H rich EVs in each tissue type. (F) Receiver operating characteristic (ROC) curve of cancer prediction for each stage.

1.4. Two-photon fluorescence lifetime imaging microscopy

1.4.1. Principles

Fluorescence is an inelastic process that occurs when a molecule absorbs a photon, bringing an electron to the excited state, and then emits a photon of slightly lower energy (due to vibrational relaxation) as the electron returns to the ground state. Each fluorescence event has a lifetime that is the time between excitation and emission when the electron is in the excited state. FLIM is a technique that characterizes fluorophores based on their mean fluorescence lifetime (τ), which defines the theoretical exponential decay distribution of time intervals between fluorophore excitation and emission [10]. In practice, with a sufficient number of photons collected, the fluorescence lifetime is determined from the response curve of fluorescence intensity over time, which takes the shape of the aforementioned exponential decay probability distribution, with time constant τ. FLIM was first developed using continuous wave lasers [10], but has since been developed for multiphoton microscopy using pulsed lasers [43]. Two-photon microscopy provides optical sectioning, reduced photodamage, and higher resolution due to the smaller excitation volume when compared to wide field or confocal fluorescence microscopy, and also uses short sub-picosecond excitation pulse widths, making it the preferred method for FLIM of biological samples [43,44].

1.4.1.1. Two-photon excitation

Two-photon fluorescence is achieved by excitation with two photons that have a combined energy equal to that of a single photon that could be used for the same transition, as shown in the Jablonski diagram in **Figure 1.6**.

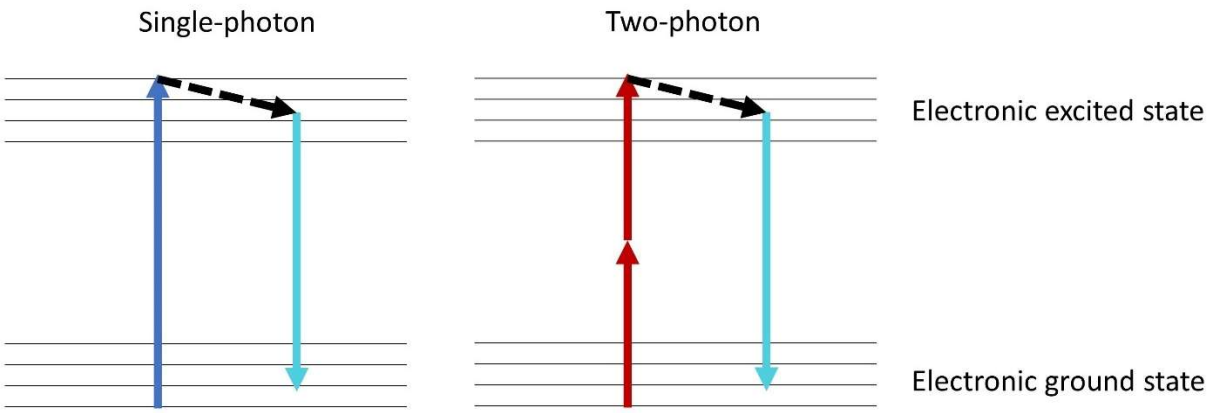

Figure 1.6: Jablonski diagram illustrating single- and two-photon fluorescence. The arrow pointing up shows the transition of an electron from the electronic ground state to the electronic excited state through absorption of one or two photons. The dashed black arrow shows loss of energy though vibrational relaxation, and the arrow pointing down shows the radiative emission of a photon of slightly less energy than the initial increase.

Mathematically, linear optics are governed by the first order interactions of the electric field with linear susceptibility ($\chi^{(1)}$), whereas nonlinear optics, such as two-photon absorption, can be described by the following power series in **Equation 1** defining the polarization (P) of a material and the higher order nonlinear susceptibilities [45].

$$P = \varepsilon_0(\chi^{(1)}E + \chi^{(2)}E^2 + \chi^{(3)}E^3 + \chi^{(4)}E^4 \ldots) \qquad \textbf{Equation 1}$$

Here, ε_0 is the permittivity of free space, E is the electric field of an incident electromagnetic wave, which can be described by **Equation 2a**, and c. c. represents the complex conjugate. The third order term polarization relating to two-photon absorption is given in **Equation 2b**.

$$E(\omega) = E_0 e^{-j\omega t} + c.c. \qquad \textbf{Equation 2a}$$

$$P^{(3)}(\omega) = \frac{3\varepsilon_0}{8}\chi^{(3)}|E(\omega)|^2 E_0 e^{-j\omega t} + c.c. \qquad \textbf{Equation 2b}$$

The effective nonlinear susceptibility, which is inversely proportional to the refractive index, is thus dependent on the square of the electric field. This is called the optical Kerr effect, where the refractive index of a material changes in response to an electric field. The imaginary component of refractive index is proportional to absorption, stemming from the complex valued

$\chi^{(3)}$ term. This value is also linearly dependent on the square of the electric field ($|E(\omega)|^2$), which means the absorption is thus proportional to the intensity of the incident light. In practice, this accounts for the small excitation volume in two-photon fluorescence compared to linear single photon fluorescence, since significant two-photon absorption only occurs in the tight focal area where intensity is the highest. This brings about the previously mentioned benefits of optical sectioning, reduced photodamage, and higher resolution [45].

1.4.1.2. Fluorescence lifetime

In the fluorescence process, the time between excitation and emission follows an exponential decay probability function for a given fluorophore at constant conditions. Mathematically, this means that the probability (p) of a photon being emitted after a given amount of time (t) follows **Equation 3** [46].

$$p(t) = \alpha e^{-(t/\tau)} \qquad \textbf{Equation 3}$$

Here, τ, the variable that defines the sharpness of the decay, is termed the fluorescence lifetime of the fluorophore, and is also equivalent to the average time the molecule remains in the excited state [44]. The α variable is a constant for normalization.

Fluorescence lifetime is defined as being inversely proportional to the sum of the rate constants of radiative processes (k_f), such as fluorescence, and non-radiative processes (k_{nr}), known as quenching, as shown in **Equation 4a.**

$$\tau = \frac{1}{k_f + k_{nr}} \qquad \textbf{Equation 4a}$$

$$\Phi_f = \frac{k_f}{k_f + k_{nr}} \qquad \textbf{Equation 4b}$$

As the rate of non-radiative processes increases, the fluorescence lifetime decreases. This additionally applies to the quantum efficiency, Φ_f, defined in **Equation 4b** as the rate of absorbed photons that result in the emission of a fluorescent photon.

An increase in the nonradiative decay constant can occur internally, primarily through molecular vibrations or rotations, or externally, by transferring the energy outside of the molecule, such as through heat transfer [44]. Internal rotation of molecules is a significant contributor to non-radiative transitions, and restriction of motion within fluorophores has thus been linked to longer fluorescence lifetimes [44]. When considering the fluorescence lifetime of a fluorophore where the non-radiative transition rate is primarily dominated by the rate of internal rotation (k_{rot}), which is defined by the Stoke-Einstein-Debye relationship in **Equation 5a**, it is clear how nanoscale variables such as temperature (T) can effect fluorescence lifetime, as shown in **Equation 5b**.

$$k_{nr} = k_{rot} = \frac{k_B T}{4\pi r^3 \eta} \qquad \textbf{Equation 5a}$$

$$\tau = \frac{1}{k_f + \frac{k_B T}{4\pi r^3 \eta}} \qquad \textbf{Equation 5b}$$

Here, k_B is the Bolzmann constant, r is radius of the molecule, and η is viscosity. This estimation of $k_{nr} = k_{rot}$ is not always appropriate, but it is helpful for conceptualizing how the fluorescence lifetime is related to the nanoscale environment of the fluorophore [44]. An external way the rotation of a molecule can be altered is binding to a protein, which would decrease the rate of rotation of the molecule and increase the fluorescence lifetime. This specific process is important for understanding NAD(P)H fluorescence lifetime, which is often separated into the longer "protein-bound" NAD(P)H fluorescence lifetime and the shorter fluorescence lifetime of "free" or unbound NAD(P)H [47].

When a group of fluorophores with different fluorescence lifetimes is probed, the corresponding probability function of time between excitation and emission will be the sum ($s(t)$) of N decaying exponentials, as shown in **Equation 6** [46].

$$s(t) = \sum_{k=1}^{N} \alpha_k e^{-t/\tau_k} \qquad \textbf{Equation 6}$$

Here, the α_k variable now represents the relative intensity of each fluorophore present.

1.4.2. Instrumentation and imaging

Two-photon fluorescence lifetime imagine is generally performed on laser scanning microscopy systems with pulsed lasers to provide fast point-scanning with short pulse durations to increase two-photon intensity and create time-resolvable data. The optical setup used for two-photon FLIM measurements is shown below in **Figure 1.7**.

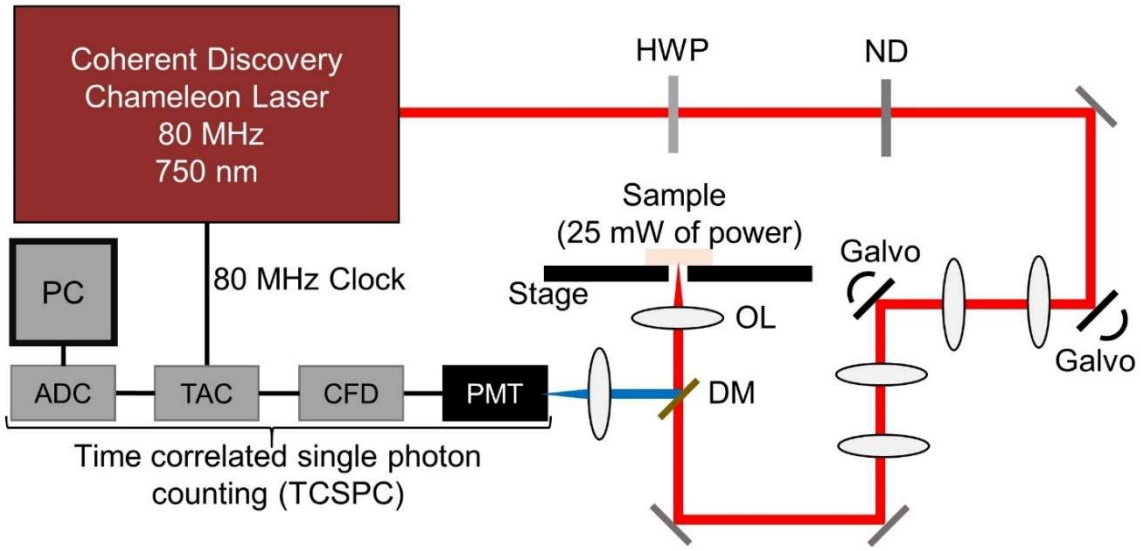

Figure 1.7: Two-photon laser scanning fluorescence lifetime imaging microscopy system diagram. The laser was tuned to 750 nm for excitation with a pulse repetition rate of 80 MHz. Light was linearly polarized with a half wave plate (HWP), and scanned on the sample with a two galvo point-scanning system. A tunable neutral density (ND) filter was used to ensure 25 mW of power was incident on the sample. Light is focused on the sample with an objective lens, which also used to collect emitted light. NAD(P)H emission, centered at 450 nm, is separated from excitation using a dichroic mirror (DM). Emission is collected by a photon-counting photomultiplier tube (PMT), thresholded by a constant fraction discriminator (CFD), clocked with a time to amplitude converter (TAC), converted to analog with an analog to digital converter (ADC), and sent to the computer (PC).

This custom setup uses a photon counting photomultiplier tube (PMT) to time-tag each collected photon based on the difference in time between the laser pulse and photon arrival at the PMT. This allows for the creation of a histogram of photon counts vs. time that approximates **Equation 6**. However, another factor to be taken into account with fluorescence lifetime measurements is the detector time response function, $d(t)$, since the detector does not provide an instantaneous response. Each pulse of the laser, occurring at a repetition rate of in radians of ω_o ($2\pi f$), will cause the emission of photons that follow the shape of $s(t)$ from **Equation 6**. This is detected as the convolution of $d(t)$ and $s(t)$, combined in **Equation 7** to represent the measured fluorescence, $f(t)$ [46].

$$f(t) = d(t) * s(t) * comb(\frac{2\pi t}{\omega_o}) \qquad \textbf{Equation 7}$$

1.4.3. Data analysis

Once the fluorescence lifetime data is acquired over space and time, the output data is a three-dimensional block of photon counts of length × width × time, and the fluorescence lifetime can be calculated based on the decay curve for each pixel. The two main fluorescence lifetime analysis techniques with regard to NAD(P)H are nonlinear least squares biexponential fitting, and phasor analysis.

1.4.3.1. Nonlinear least squares fitting

When the number of distinct fluorescence lifetimes in a sample (N from **Equation 6**) is greater than one, the process of determining the fluorescence lifetimes and normalization coefficients from the experimental data is not fully defined. However, a nonlinear least squares fitting algorithm can be used to estimate these values. Often, NAD(P)H fluorescence lifetime can be approximated to a biexponential model ($N = 2$) of one shorter, free lifetime (τ_1), and one longer, protein-bound lifetime (τ_2). The pros and cons of this assumptions are addressed in the next two

sections (**Section 1.4.3.2** and **Section 1.4.4**) generally and in **Section 2.6** specifically for EV image analysis.

The normalization constant α_k from **Equation 6** now takes meaning as the bound ratio, β, giving the proportion of photons fitting into the protein bound lifetime decay compared to the free lifetime decay, shown in **Equation 8a**, where $s'(t)$ is the fit fluorescence decay. Initial guesses for the three variables (τ_1, τ_2, β) are input, and then the error between the measured fluorescence and the fit model is minimized in an iterative method. This error is calculated using a metric such as the sum of the squared error (SSE), shown in **Equation 8b**.

$$s'(t) = (1 - \beta)e^{-t/\tau_1} + \beta e^{-t/\tau_2} \quad \textbf{Equation 8a}$$

$$SSE = \left(\sum_{t=0}^{t=\frac{2\pi}{\omega_0}} f(t) - d(t) * s'(t)\right)^2 \quad \textbf{Equation 8b}$$

Minimizing the SSE is just one method of optimization, and there are additionally a variety of different minimization algorithms. The drawbacks of this technique are mostly due to error in fitting and results that may depend on the optimization algorithms, which can differ based on the user, causing disparities in calculated values between different groups. However, the benefit of nonlinear least squares fitting to fluorescence lifetime data of NAD(P)H is that it provides three tangible outputs (τ_1, τ_2, and β) and that they are easily interpretable and meaningful.

1.4.3.2. Phasor analysis

Another technique for fluorescence lifetime analysis is phasor analysis, which provides a simpler, linear analysis of fluorescence lifetime data, but may prove harder to interpret. Phasor analysis aims to characterize the unknown variable $s(t)$ in **Equation 7** with measured $f(t)$ and knowledge of $d(t)$ and ω_o. **Equation 6** represents the time domain, but can easily be converted into the frequency domain (**Equation 9a**) and rearranged (**Equation 9b**) [46,48].

$$F(\omega_o) = D(\omega_o)S(\omega_o) \quad \textbf{Equation 9a}$$

$$S(\omega_o) = F(\omega_o)/D(\omega_o) \quad \textbf{Equation 9b}$$

Next, the frequency domain variables of measured fluorescence ($F(\omega_o)$) and detector response function ($D(\omega_o)$) are calculated from their known time domain counterparts and split into a normalized real (g) and imaginary (s) basis as shown in **Equations 10(a-c)** and **Equations 11(a-c)** [46,48].

$$F(\omega_o) = f(t)\cos(\omega_o t) + jf(t)\sin(\omega_o t) \quad \textbf{Equation 10a}$$

$$g_f = \frac{f(t)\cos(\omega_o t)}{\int f(t)} \quad \textbf{Equation 10b}$$

$$s_f = \frac{f(t)\sin(\omega_o t)}{\int f(t)} \quad \textbf{Equation 10c}$$

$$D(\omega_o) = d(t)\cos(\omega_o t) + jd(t)\sin(\omega_o t) \quad \textbf{Equation 11a}$$

$$g_d = \frac{d(t)\cos(\omega_o t)}{\int d(t)} \quad \textbf{Equation 11b}$$

$$s_d = \frac{d(t)\sin(\omega_o t)}{\int d(t)} \quad \textbf{Equation 11c}$$

These basis values are then used to define the frequency domain fluorescence decay of the sample ($S(\omega_o)$), and decompose $S(\omega_o)$ into its own normalized real (g) and imaginary (s) basis, as shown in **Equations 12(a-c)** [46,48].

$$S(\omega_o) = \frac{g_f + js_f}{g_d + js_d} = g_s + js_s \quad \textbf{Equation 12a}$$

$$g_s = \frac{g_f g_d + s_f s_d}{(g_d)^2 + (s_d)^2} \quad \textbf{Equation 12b}$$

$$s_s = \frac{-g_f s_d + s_f g_d}{(g_d)^2 + (s_d)^2} \quad \textbf{Equation 12c}$$

These two basis components should fall within the unit circle as shown in **Figure 1.8**, though experimentally due to noise occasionally values fall outside the circle. Any sum of exponential decays can be fully described by these two basis components, and the mean fluorescence lifetime of the sum of decays is calculated with **Equation 13** [46,48].

$$\tau = \frac{s_l}{\omega_o g_l} \qquad \textbf{Equation 13}$$

Figure 1.8 shows five different fluorescence lifetime profiles. In red, τ_1 represents a pure fluorescence lifetime around 0.6 ns; τ_2 in light blue is a pure fluorescence around 3 ns; τ_3 in dark blue is a pure fluorescence lifetime around 4 ns; τ_4 and τ_5 both represent mixtures with mean fluorescence lifetimes of 1.6 ns [46].

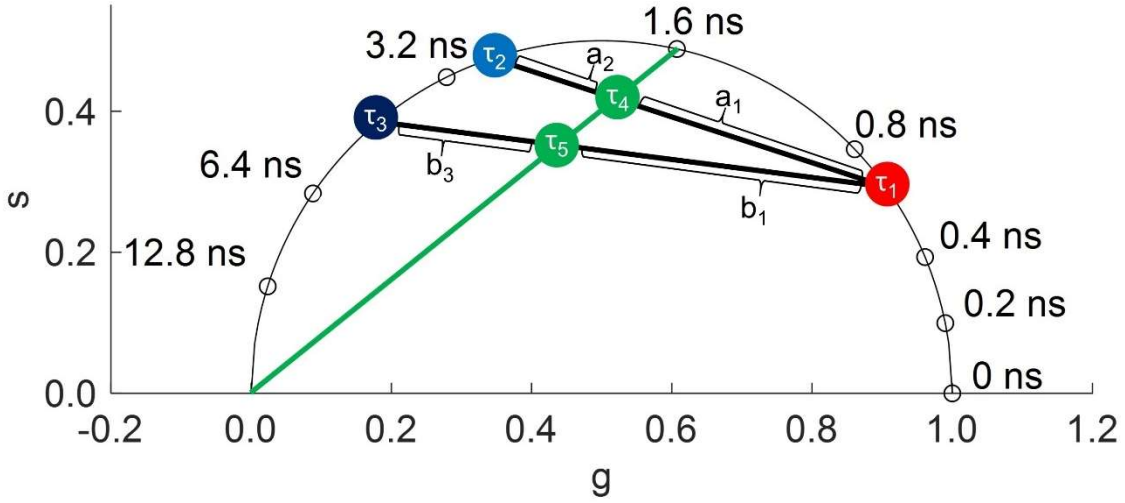

Figure 1.8. Example phasor plot with 5 fluorescence lifetime profiles represented [46]. Measured fluorescence lifetime profiles are decomposed into a two component basis (g and s) that are visualized on phasor plots such as this one.

Mixtures of multiple fluorescence lifetimes are represented at a location between the fluorescence lifetimes present, weighted by relative intensity, α, given in **Figure 1.8** as a_1, a_2, b_1, and b_3. For example, the τ_4 location represents a mixture of τ_1 and τ_2, where the ratio of the intensity of fluorophores with fluorescence lifetime of τ_1 to fluorescence lifetime τ_2 is a_1:a_2. The

usefulness of the phasor plot is highlighted by the ability to distinguish τ_4 and τ_5 as having different fluorescence lifetime components, despite having the same mean fluorescence lifetime. Similar fluorescence lifetime profiles will cluster together on the scatterplot. The mean fluorescence lifetime of a decay, τ, is proportional to s/g (**Equation 13**), so points falling on the same line passing through the origin have the same τ value.

When compared to nonlinear least squares bi-exponential fitting, the main benefits of phasor analysis for NAD(P)H lifetime calculation is that it is a linear problem that eliminates the assumption of the bi-exponential decay. Furthermore, phasor analysis does not introduce any fitting error and is faster. **Table 1.1** summarizes the main characteristics of both techniques.

Table 1.1: Comparison of nonlinear least squares bi-exponential fitting and phasor analysis for fluorescence lifetime decay characterization.

	Nonlinear least squares	**Phasor**
Number of exponential decays	bi-exponential	n-exponential (n>0)
Order of computation	nonlinear	linear
Fitting/optimization error	yes	no
Speed	slower	faster
Outputs	τ_1, τ_2, β	g, s, τ

1.4.4. NAD(P)H autofluorescence and fluorescence lifetime imaging

As previously stated, reduced nicotinamide adenine dinucleotide (NADH) and reduced nicotinamide adenine dinucleotide phosphate (NADPH) are autofluorescent cofactors present in abundance in cells [49]. The molecules exhibit similar excitation and emission spectra, since their structure only differs by one phosphate group. Because of this similarity, their autofluorescence intensity alone cannot be separated, and is thus referred to as "NAD(P)H" [49]. Since there is about 10 times more NAD+/NADH in cells than NADP+/NADPH [49], it is often approximated that cellular NAD(P)H autofluorescence imaging is dominated by NADH, although it is important to

note that this ratio depends on the cell type and its metabolic state. The structures of NAD+, NADH, NADP+, and NADPH are shown in **Figure 1.9** below [50].

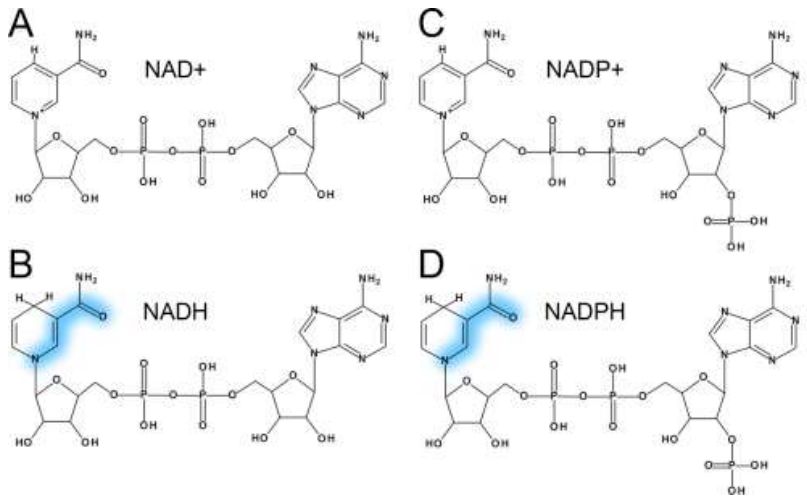

Figure 1.9: Molecular structures of NAD+, NADH, NADP+, and NADPH [50].

NAD(P)H autofluorescence, along with FAD autofluorescence, has been widely used in cell and tissue imaging to calculate the ORR, which as previously stated is used to quantify metabolic function [41,42,51]. The ORR can be calculated from the autofluorescence intensity of FAD and NAD(P)H in multiple ways, depending on researcher preference, as given in **Equation 14a-c**. ORR calculations can be normalized to create a value between 0 and 1 (**Equation 14a** [9,41]), or give the relative autofluorescence of the two cofactors without normalization (**Equation 14b** [51], **Equation 14c** [42]). Previous EV work has used the normalized equation in **Equation 14a** [9].

$$ORR = \frac{FAD}{FAD + NAD(P)H} \qquad \textbf{Equation 14a}$$

$$ORR = \frac{NAD(P)H}{FAD} \qquad \textbf{Equation 14b}$$

$$ORR = \frac{FAD}{NAD(P)H} \qquad \textbf{Equation 14c}$$

Autofluorescence intensity is a very useful parameter, however NAD(P)H autofluorescence intensity does not provide complete information on the state or concentration of NAD(P)H. It has been shown that protein-bound NAD(P)H has a larger quantum yield than free NAD(P)H by approximately 10 times (consistent with **Equation 4b**); thus autofluorescence intensity is not directly proportional to NAD(P)H concentration when there is a mix of free and protein-bound NAD(P)H [49,52]. Fortunately, fluorescence lifetime imaging microcopy (FLIM) can be used to better understand the state of NAD(P)H within samples since protein-bound and free NAD(P)H exhibit different characteristic fluorescence lifetimes [47].

The fluorescence lifetime of NAD(P)H in cells and tissues has been widely studied [41,42,53-56], and it has been found that when bound to a protein, NAD(P)H exhibits a relatively longer fluorescence lifetime of approximately 1.5-6 ns, whereas free NAD(P)H exhibits a characteristically shorter fluorescence lifetime of approximately 0.3-0.8 ns [40,47]. This matches well with the presented theory in **Section 1.4.1.2**, since the restriction of motion that occurs with protein binding will decrease the k_{nr} and increase the fluorescence lifetime of a molecule (**Equation 4a**). Two-photon FLIM of NAD(P)H has been used to study a variety of biological phenomena such as apoptosis dynamics [53,54], brown adipose tissue metabolism [41], and assessing tumor margins in lung cancer [57].

Another remaining issue related to imaging NAD(P)H is that NADH and NADPH cannot be distinguished with autofluorescence alone. It has been found that while free NADH and NADPH in a buffer solution have indistinguishable fluorescence lifetimes, protein-bound NADH has a mean fluorescence lifetime of approximately 1-3 ns whereas protein-bound NADPH has a mean fluorescence lifetime of approximately 2-6 ns [40,52,58]. In addition, the fluorescence lifetime of NADH differs slightly when it is bound to different enzymes such as malate

dehydrogenase (MDH) and lactate dehydrogenase (LDH). NADH bound to those enzymes has a shorter fluorescence lifetime than NADPH bound to glucose-6-phosphate dehydrogenase (G6PDH) [58]. This may be because G6PDH has about twice the molecular weight of MDH and LDH [59], since theoretically the larger size of G6PDH will decrease the k_{rot} value and increase τ of the fluorophore (**Equation 5a,b**). Thus, FLIM can provide insight into the enzymatic makeup of biological material as it relates to bound and free NAD(P)H.

Two-photon FLIM of NAD(P)H has been established as a valuable technique for imaging and characterizing cells and tissues in cancer and other diseases, and NAD(P)H has been determined to be a molecule of interest in EVs. For these reasons, it follows that FLIM has the potential to probe the state of NADH and NADPH in EVs and provide label-free characterization of single EVs based on the fluorescence lifetime of the two cofactors.

2. EXPERIMENTAL METHODS FOR IMAGING NAD(P)H IN EXTRACELLULAR VESICLES

2.1. Motivation: label-free single EV analysis

As previously mentioned, many have called for advancements in single EV analysis techniques in order to assess the spatial, molecular, and functional heterogeneity of EVs [8]. The overall goal of this work was to explore the usefulness of FLIM of NAD(P)H for examining EVs and determine appropriate procedures for the sample preparation, imaging, and image analysis. Previous work using SLAM microscopy showed initial promise for nonlinear imaging of EVs [9,37], but it was hypothesized that FLIM would provide new and useful information about the NAD(P)H content, as well as another means of label-free functional single EV analysis.

2.2. Cell culture and EV isolation

EVs were isolated from human breast cancer epithelial cells, MDA-MB-231 (ATCC, HTB-26, USA) to allow for comparison with previous studies using SLAM to characterize EVs in breast cancer [9]. Cells were grown at 37°C and 5% CO_2 in phenol red-free Dulbecco's Modified Eagles Medium (DMEM, Gibco, Waltham, MA) supplemented with 25 mM glucose, 4mM L-glutamine, 25 mM HEPES, 10% heat-inactivated Fetal Bovine Serum (FBS, GE Healthcare Life Sciences, HyClone Laboratories, Logan, UT), and 1% streptomycin-penicillin antibiotic solution (Thermo Fisher Scientific, Waltham, MA) [46].

When cells reached 70% confluency, media was removed and cells were rinsed twice with sterile 1x Phosphate Buffered Saline (PBS, GE Healthcare Life Sciences, HyClone Laboratories, Logan, UT) and placed in serum- and phenol red-free DMEM supplemented with 4mM L-glutamine, 25 mM HEPES, 1% streptomycin-penicillin antibiotic solution (Thermo Fisher Scientific, Waltham, MA), and 25 mM glucose. Cells were returned to the incubator at 37°C and

5% CO_2 to collect output EVs in the serum-free media. After an incubation time of 48 hours, the media was removed from cells, transferred into 50 mL protein LoBind conical tubes (Eppendorf, Hauppauge, NY), and centrifuged sequentially at 800×g for 10 min to pellet cells, at 2,000×g for 30 min to pellet particles larger than 1000 nm, and at 12,000×g for 60 min to pellet EVs. All centrifugation steps were performed at 4°C and samples were kept on ice in between steps. The final EV pellet was resuspended in 10 µL of sterile PBS per each 10 mL of initial cell media in PCR clean protein LoBind tubes (Eppendorf, Hauppauge, NY). This serial differential ultracentrifugation procedure was followed based on previous similar studies and established isolation protocols [9,16,19-21]. The EV isolation and sample preparation procedure is presented in **Figure 2.1** [46].

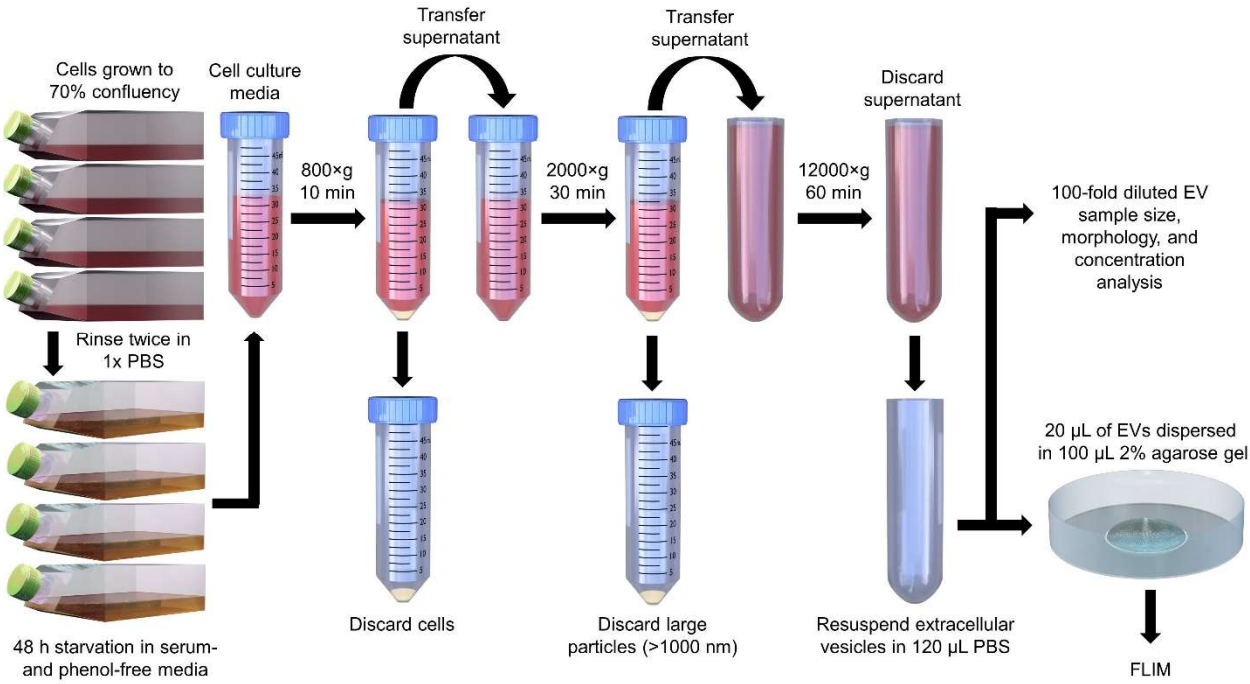

Figure 2.1. Schematic illustration of extracellular vesicle (EV) isolation from cell culture fluid and sample preparation prior to imaging [46]. EV samples were derived from the serum-free media after the cells were maintained in T175 cell culture flasks for 48 hours. EVs were concentrated and isolated by serial differential ultracentrifugation. Isolated EVs were suspended in phosphate buffer solution (PBS) with a portion of the sample set aside for concentration and morphological characterization and the rest of the sample embedded in 2% agarose gel for imaging with fluorescence lifetime imaging microscopy (FLIM).

2.3. EV sample characterization

For morphological validation and characterization, a portion of isolated EV samples were imaged with TEM (Phillips CM200, FEI Company, Thermo Fisher Scientific, Hillsboro, OR). Carbon-coated copper grids were placed in the diluted solution of EVs resuspended in PBS for 3 min, then gently dabbed to dry on sterile filter paper. Next, the grids were negatively stained with 2% uranyl acetate for 30 seconds, after which the excess uranyl acetate solution was again removed with sterile filter paper. Grids were then left to dry for 10-15 min prior to imaging [46]. Multiple EV TEM images (**Figure 2.2(a)**) showed the expected cup-like morphology and lipid-bilayer membrane enclosed spheres [60].

For enumeration and size distribution, NTA (Nanosight, Malvern, UK) was performed on a portion of isolated EVs. From the initial solution of isolated EVs, a 10 μL aliquot was diluted into 990 μL sterile PBS. EV sizes and concentrations were calculated using NTA software and then adjusted to calculate the number of EVs per initial volume of cell culture media [46]. NTA size distribution consistently showed particles ranging from around 50 to 600 nm in diameter with most of the particles concentrated in the 100 to 300 nm diameter range; an example histogram of estimated particle sizes is shown in **Figure 2.2(b)** [46].

EVs were also analyzed with Raman spectroscopy (LabRAM HR 3D, Horiba Scientific, Edison, NJ) for biochemical characterization. Three samples of 10 μL each were left to dry on glass coverslips overnight and imaged the following day. Spectroscopy was performed with 532 nm laser excitation, filter optical density of 0.3 OD, 100 μm slit, 300 μm confocal aperture, and a grating centered at 2000 cm^{-1} with 300 g/mm. Spectrum measurements were averaged over 10 s with 0.1 s acquisition time [46]. Previous studies using Raman spectroscopy have not examined EVs from MDA-MB-231 cell culture, but various spectral features of the presented data match

with the biochemical profiles found in previous studies of EVs derived from other cells and tissues (**Figure 2.2(c)**) [28-30,35].

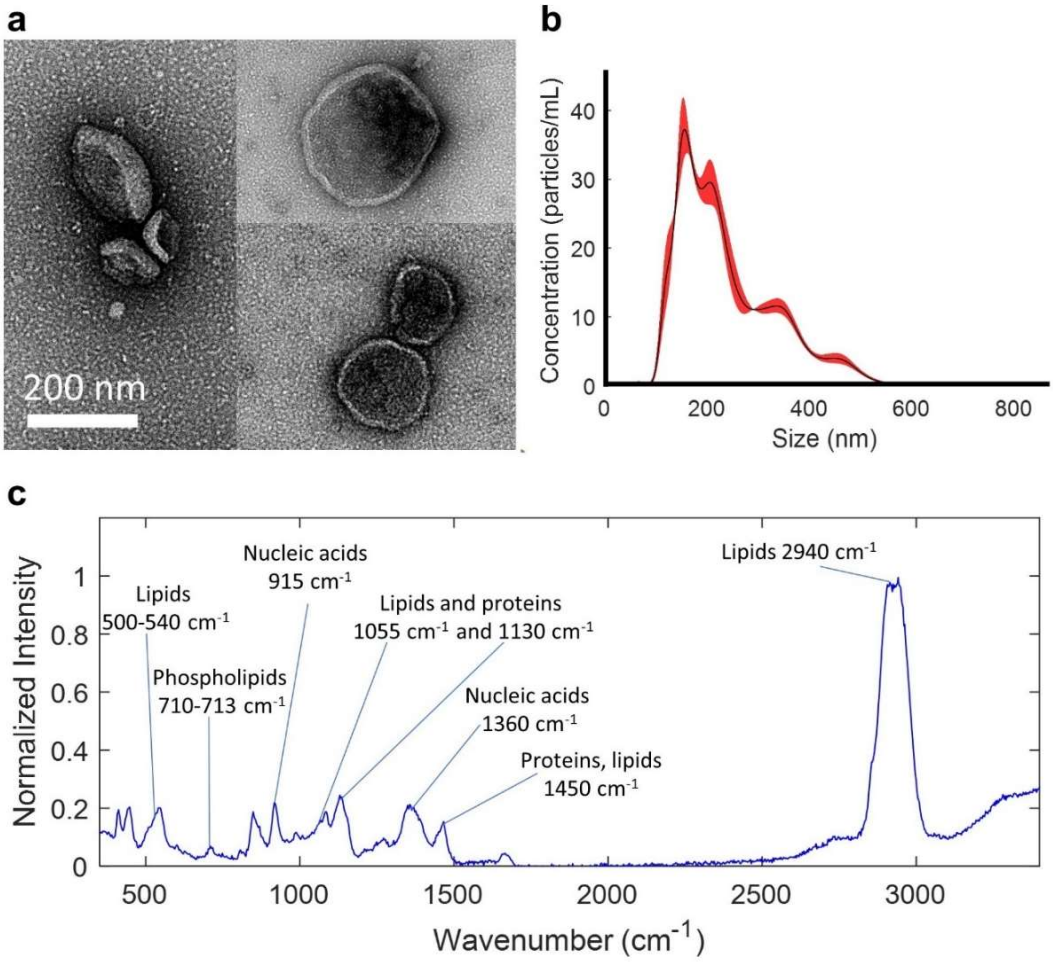

Figure 2.2. Morphological and biochemical characterization of extracellular vesicles (EVs) [46]. (a) Transmission electron microscopy (TEM) of multiple EVs that show either cup-like (*left*) or a more open morphology (*right*). (b) Representative concentration density of EVs by size as determined by nanoparticle tracking analysis (NTA), given in concentration of EVs per mL of cell culture media used for isolation. (c) Averaged and normalized Raman spectrum of EVs that were dried on a coverslip overnight; n=3. Common peaks are annotated based on previous Raman characterizations of EVs [28-30,35].

2.4. Embedding and imaging

In order to accumulate multiple frames over the timespan of a few minutes, which is needed to collect sufficient autofluorescence signal, EVs must be embedded in a material to stabilize them and prevent movement or diffusion. Previous work imaging isolated EVs with nonlinear optical

microscopy used glycerol [9], however some have hypothesized that EVs contain the metabolic pathways to metabolize glycerol [61], which could taint results. In order to determine the optimal embedding material, EVs were imaged in a 2% agarose gel, glycerol, and Matrigel, as shown by NAD(P)H intensity images in **Figure 2.3**. It was determined that glycerol was not viscous enough because some EVs diffused over the course of imaging (an example trail is marked by the red arrow), and that the background signal from Matrigel was too high. This led to a 2% agarose gel being used for EV embedding and imaging throughout the study.

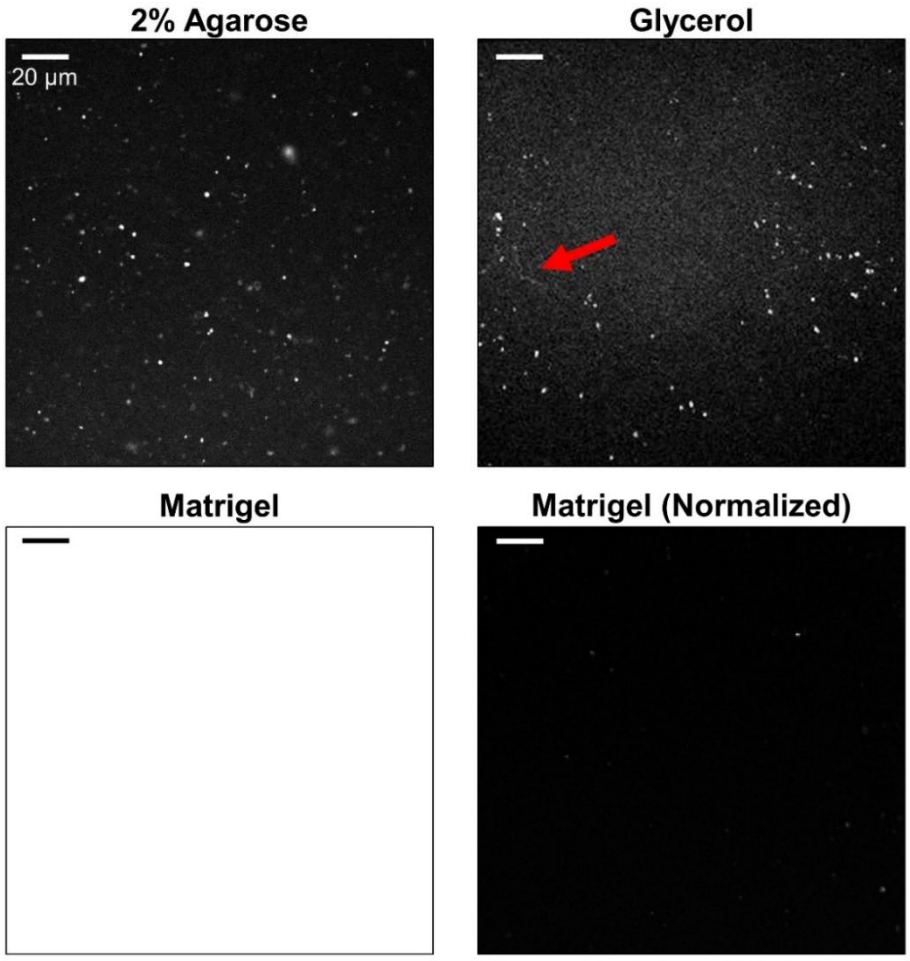

Figure 2.3: Extracellular vesicle (EV) NAD(P)H intensity imaged in different embedding material. EVs derived from MDA-MB-231 cells are shown in 2% agarose gel, glycerol, and Matrigel, all using the same intensity scale. Since the background signal from Matrigel overpowers the NAD(P)H signal from most EVs, the Matrigel image is also shown on a normalized scale. A red arrow marks the path of a diffusing EV in the glycerol sample.

EVs were embedded in a 2% agarose gel on a glass-bottom coverslip (MatTek P35G-0-10-C) and set in the refrigerator at 4°C for a few minutes for the gel to solidify prior to imaging. Samples were plated in glass bottom imaging dishes to allow for illumination and detection from below. All samples were imaged within an hour after embedding and not stored long term, except those explicitly mentioning storage that were stored in PBS and embedded immediately after thawing. EV and samples were imaged using the previously described custom laser scanning multiphoton setup with FLIM capabilities [55] given in **Figure 1.7**.

For each pixel within the image, photons were tagged and binned by the time delay between the laser pulse and when the photon arrived at the detector, creating a histogram of photon counts vs. time for each pixel, as described in **Section 1.4.2**. A time bin size of 8 ps was used for all reported experiments. Since the NAD(P)H fluorescence signal from EVs is relatively low, 20 frames were accumulated per field of view over approximately 2 min. The area of each field of view was 180×180 μm^2, or 512×512 pixels. To image a sufficient number of EVs for analysis, 16 fields of view were acquired per sample, which took around 30 min in total per sample [46].

2.5. Image segmentation with blob detection algorithm

A blob detection algorithm was used to segment single EVs from raw NAD(P)H intensity images. Intensity images were created by taking the average value of each photon count histogram. Blob detection is a commonly used feature detection algorithm to detect round objects of different sizes [62]. Image processing was performed using Matlab 2018 (Mathworks, Natick, MA), and the process for creating a segmentation mask for EVs is shown in **Figure 2.4** [46].

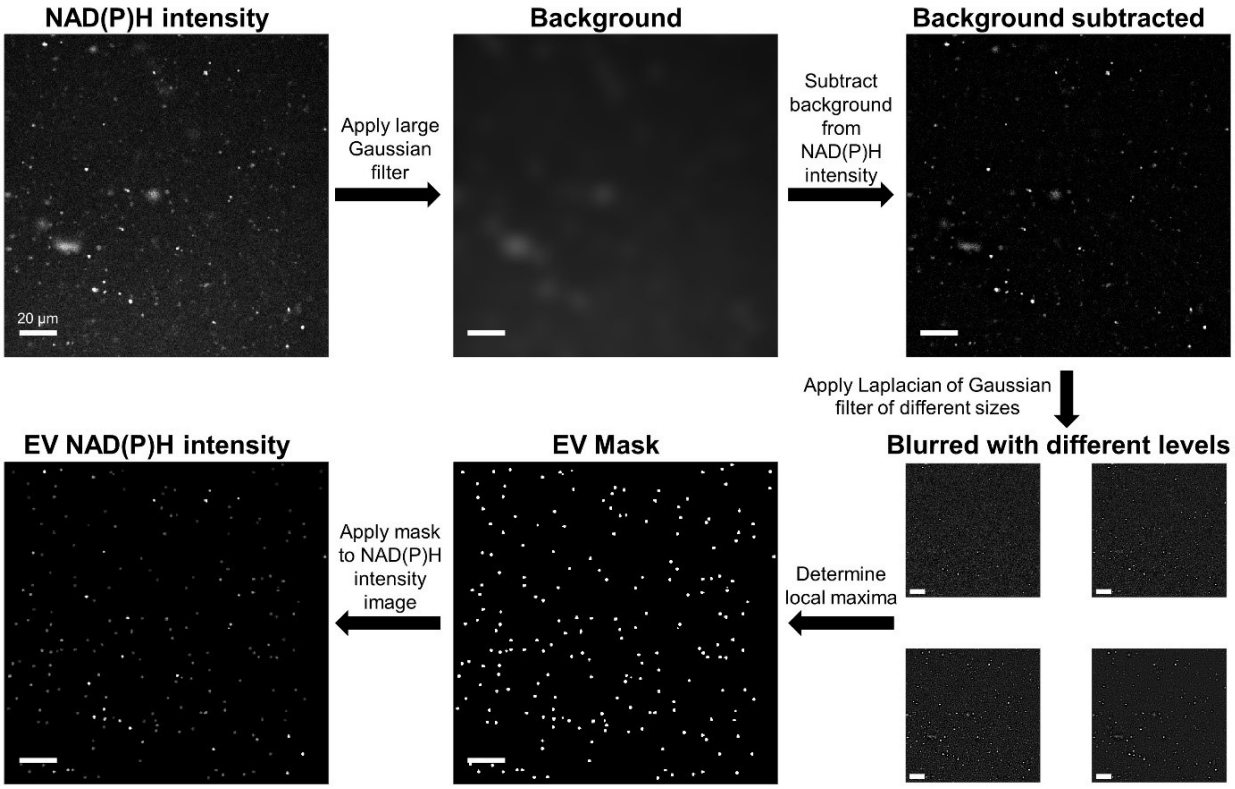

Figure 2.4. Schematic of extracellular vesicle (EV) segmentation of NAD(P)H autofluorescence intensity image using a blob detection algorithm [46]. A large Gaussian filter was applied and then subtracted from the original intensity image to adjust for nonuniformity in the background. Next, multiple Laplacian of Gaussian filters of different sizes/levels were applied to the image to highlight local maxima of corresponding sizes. A 3D local maxima filter was applied to a stack of images filtered at different levels to create a mask of EVs of different sizes. A threshold was applied to only segment local maxima that exceed the background noise as the center of EVs to create a binary EV mask. Finally, this binary EV mask was multiplied with the original intensity image to display the intensity of each segmented EV. Scale bars represent 20 µm.

Figure 2.4 is a good example of how most images are segmented, however occasionally there are air bubbles, coverslip scratches, or other debris in the sample that is not related to the EV content. In cases where there is a large bright region in the image being process, there is another step in the image processes that highlights "high noise regions" that are much brighter than the rest of the sample and excludes them from analysis. The processing algorithm for excluding high noise regions is shown in **Figure 2.5**.

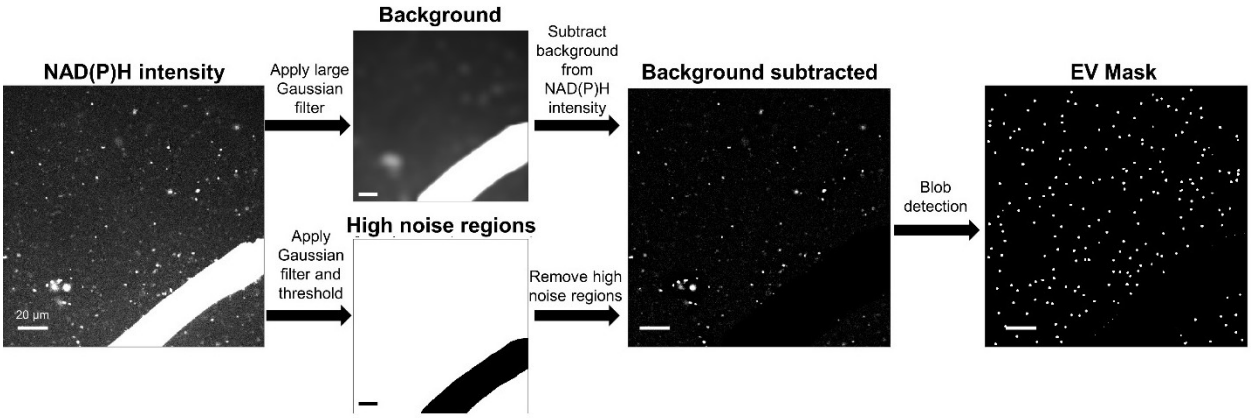

Figure 2.5: Exclusion of high noise regions from blob detection algorithm. In order to remove areas of high signal that do not originate from extracellular vesicles (EVs), a Gaussian filter is applied to NAD(P)H intensity images, and large areas with intensity values greater than 20 times the median value are excluded from analysis. After exclusion, the rest of the image can go through the rest of the blob detection algorithm and be used for analysis.

2.6. Lifetime analysis of single EVs

After the EV segmentation mask was created, the photon count histograms of each pixel within a segmented EV were binned to one representative decay per EV to increase signal. Two representative EV fluorescence decays (*blue* and *cyan*) are shown in **Figure 2.6**, along with fluorescence decays from a bi-exponential fit (*red*) and the fluorescence decay from the mean lifetime from phasor analysis (*green*) in **Figure 2.6** calculated as discussed in **Sections 1.4.3.1** and **1.4.3.2**.

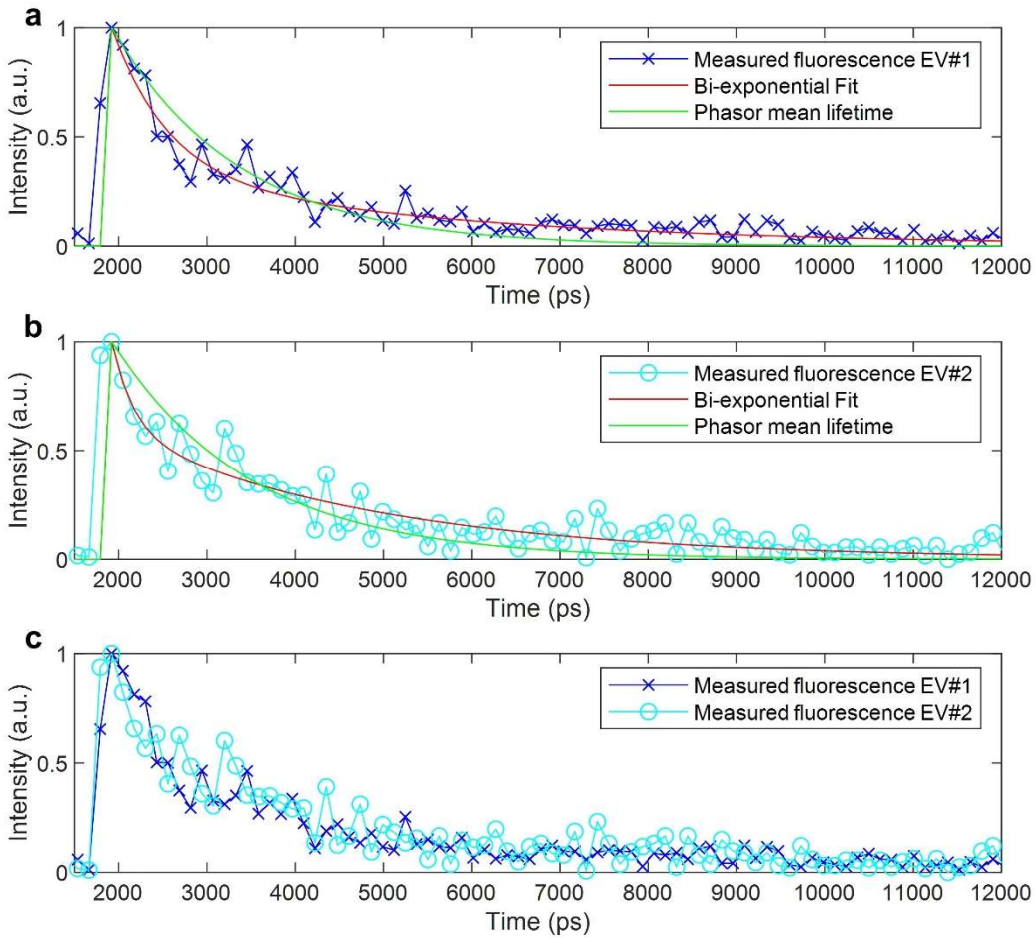

Figure 2.6: Representative comparison of measured fluorescence, nonlinear least squares fitting, and phasor analysis for extracellular vesicles. Measured fluorescence for (a) EV#1 (*blue*) and (b) EV#2 (*cyan*), with the nonlinear least squares bi-exponential fitting (*red*), and phasor analysis (*green*) for two different extracellular vesicles (EVs). (c) Comparison of just the measured fluorescence decays of the two EVs.

By visual examination, it is easy to assume from **Figure 2.6(a)** and **Figure 2.6(b)** that the bi-exponential fit is superior, since it appears to track the measured fluorescence better. This, however, is deceiving. In part, it is deceiving due to the fact that phasor analysis only provides one mean lifetime and does not aim to recreate the original decay, but instead aims to fully characterize it in a two component basis, which happen to allow the calculation of one mean fluorescence lifetime. The mean fluorescence lifetime from phasor analysis approximates the shape of the decay as well as a single-exponential fit can; which is a mathematically valid observation since it is the solution to a linear problem. Furthermore, from examination of **Figure 2.6(c)**, it is clear that the

two EVs have similar fluorescence decays, and thus should have similar fluorescence lifetime profiles. The variables defining the two models and the SSEs are listed in **Table 2.1**.

Table 2.1: Comparison of phasor analysis and bi-exponential nonlinear least squares fitting outputs for fluorescence lifetime decays of two EVs.

Method	**Variable**	**EV#1**	**EV#2**
Phasor analysis	τ_{mean} (ns)	1.423	1.560
	g, s	0.4485, 0.3179	0.4565, 0.3549
	SSE	2.72	2.14
Bi-exponential NLS fit	τ_1 (ns)	0.623	0.241
	τ_2 (ns)	3.778	2.971
	β	0.3375	0.5965
	SSE	2.52	2.05

As expected, the SSE is larger for the phasor analysis, however, it is still within 10% of the SSE of the bi-exponential fit, which is consistent with comparison of many other EVs. The concerning data presented in **Table 2.1** is that the fluorescence lifetime values τ_1 and τ_2 from the bi-exponential nonlinear least squares fit are very different for the two EVs. This is likely due to overfitting of the data, which cannot happen with the phasor approach. Phasor analysis resulted in similar mean lifetimes and g and s basis values. With enough photons collected in data from cells or tissues, there is much less noise, and less concern for overfitting a nonlinear least squares model. However, with the noisy EV data, there does not appear to be enough data to conclusively pinpoint valid bound and free fluorescence lifetimes using nonlinear least squares fitting.

Furthermore, the biexponential fluorescence lifetime fit is based on the assumption of two distinct "free" and "bound" lifetime decays. For the most part, this works well in cells since we have much more knowledge about the states of NADH and NADPH in cells. But, a bi-exponential model should not be applied to EV NAD(P)H FLIM until more is known about the state of NADH and NADPH in EVs and which species are dominating the fluorescence decay curves. Thus, it was determined that the optimal method of fluorescence lifetime analysis of the collected EV data was to calculate the mean fluorescence lifetime, τ, of each EV using the phasor approach for FLIM.

Phasor analysis of corresponding cell FLIM images was also performed to allow for direct comparison of the data sets.

2.7. Discussion

The presented data and methods show how FLIM can be used to image and characterize NAD(P)H autofluorescence originating from single EVs. Standard isolation (**Figure 2.1**) and validation (**Figure 2.2**) techniques were used in conjunction with a FLIM system (**Figure 1.7**) that has previously been used to image NAD(P)H fluorescence lifetime in cells and tissues [55]. However, in order to achieve FLIM of the NAD(P)H of EVs, development of new methods of EV embedding (**Figure 2.3**) and image processing (**Figure 2.4, Figure 2.5**) were necessary. It was also found that for the present setup, phasor analysis was superior since a bi-exponential nonlinear least squares fit appeared to be overfitting (**Figure 2.6**, **Table 2.1**). This overfitting may not be the case in future work if a higher SNR is achieved; however, it is important to first establish how valid the bi-exponential fit model is in EVs before applying it, and it is not yet fully understood how the NAD(P)H content of EVs differs from that of cells, though the data presented throughout do provide a good starting point.

Overall, the presented novel procedure for imaging and characterizing EVs with FLIM of NAD(P)H provided acceptable and meaningful results, more of which will be presented throughout this thesis. It is, however, important to note that there is still room for innovation and improvement on these techniques. For example, validation of the blob detection algorithm with EV-sized beads with known fluorescence lifetimes and with EVs from a variety of different sources and samples may enable more robust and accurate analysis. Wide-field FLIM of NAD(P)H could also be used to characterize a population of EVs, although the single EV capabilities would be lost.

One recent advancement in the application of FLIM to diagnostics is the creation of a microfluidic culture device for imaging CTCs derived from patient blood samples [63], which could additionally image EVs and examine the roles EVs play in CTC cluster formation. Furthermore, microfluidic devices [64] and micro-flow cytometry [36] have been employed in EV imaging and analysis, and could be paired with FLIM for label-free higher throughput functional imaging of single EVs. Microfluidic EV technology has also contributed to a decrease in the sample volume needed for analysis and is expected to continue to advance the field to faster, more reliable, lower cost solutions [8].

3. NAD(P)H FLUORESCENCE LIFETIME OF EXTRACELLULAR VESICLES

3.1 Motivation: Understanding EV NAD(P)H fluorescence lifetime

There exists no precedent for characterizing the fluorescence lifetime of NAD(P)H in EVs. It is important to establish the feasibility and repeatability of this imaging, in addition to determining what types of EVs can be imaged and if data is repeatable. Furthermore, many have hypothesized that EVs are heterogeneous, and previous work has shown that NAD(P)H intensity of EVs is heterogeneous [9], however until this work it was unknown what the fluorescence lifetime distribution within a population of EVs would be.

3.2 Heterogeneity of EV fluorescence lifetimes

FLIM provides single EV resolution, which can reveal information about the heterogeneity of EVs within each sample. A segmented fluorescence lifetime-weighted image of EVs derived from MDA-MB-231 cells shows dozens of EVs with NAD(P)H fluorescence lifetimes between around 0.8 ns and 2.2 ns (**Figure 3.1(a)**). To demonstrate the heterogeneous nature of individual EVs, two example decays, one relatively short and one relatively long, from EVs with similar NAD(P)H intensities are shown in **Figure 3.1(b,c)**. In **Figure 3.1(d)**, each EV was plotted as a single point on the phasor plot [46]. Approximate values of protein-bound NADH and NADPH, and free NAD(P)H were labelled according to previous studies [40,58].

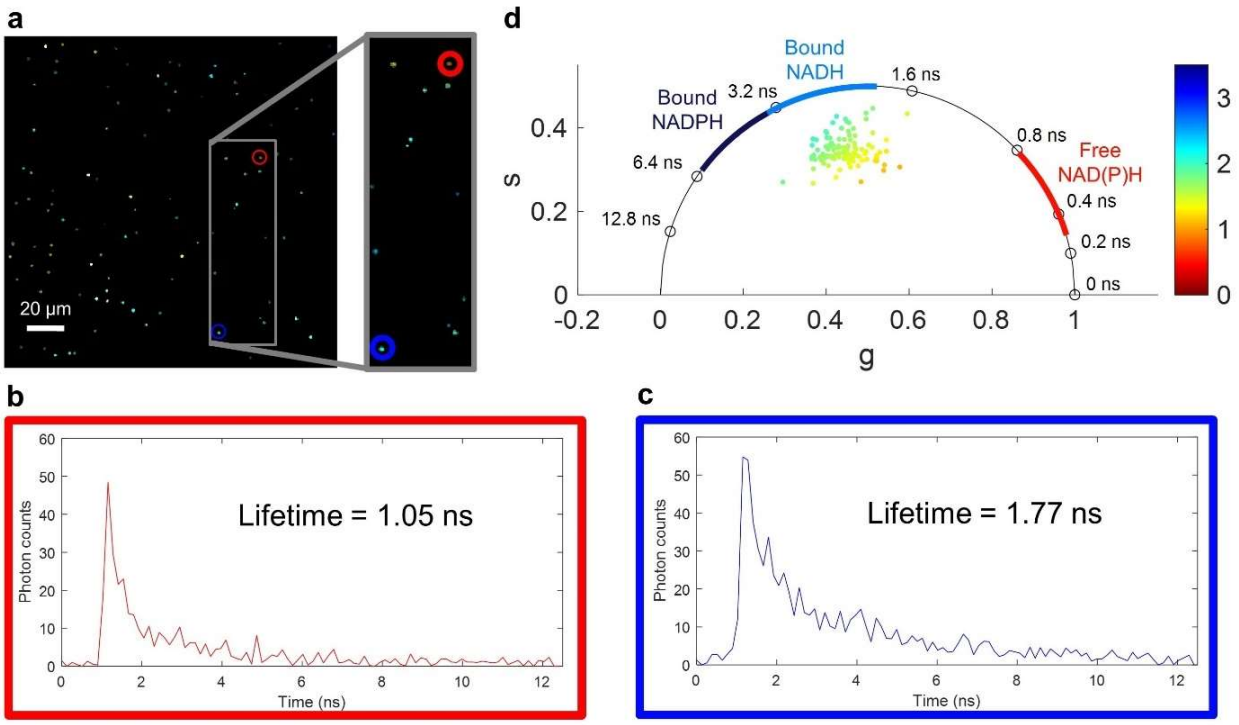

Figure 3.1. Heterogeneity of fluorescence lifetimes in cell-derived extracellular vesicles (EVs) [46]. (a) Fluorescence lifetime-weighted intensity image of EVs. The brightness of a pixel corresponds to the autofluorescence intensity and the color corresponds to fluorescence lifetime in ns, using the same fluorescence lifetime scale in panel (d). Example of fluorescence decay curve of a relatively shorter (b) and longer (c) fluorescence lifetime corresponding to the EV in the red (b) and blue (c) circles in panel (a). (d) Phasor plot of the frequency components of the fluorescence lifetimes of the EVs in (a). Each point on the plot represents a single EV from the image in (a). The color of the point represents the fluorescence lifetime of the EV in ns. Approximate fluorescence lifetime values of protein-bound and free NAD(P)H based on previous studies are indicated [40,58].

3.3 Negative Control

To ensure that the particles being imaged with FLIM were cell-derived EVs, the differential centrifugation, sample preparation, and image processing procedures were performed on cell culture media that was not incubated on cells. This negative control (**Figure 3.2**) shows significantly fewer particles (averaging 1 per frame) compared to data taken on samples with cell-derived EVs [46].

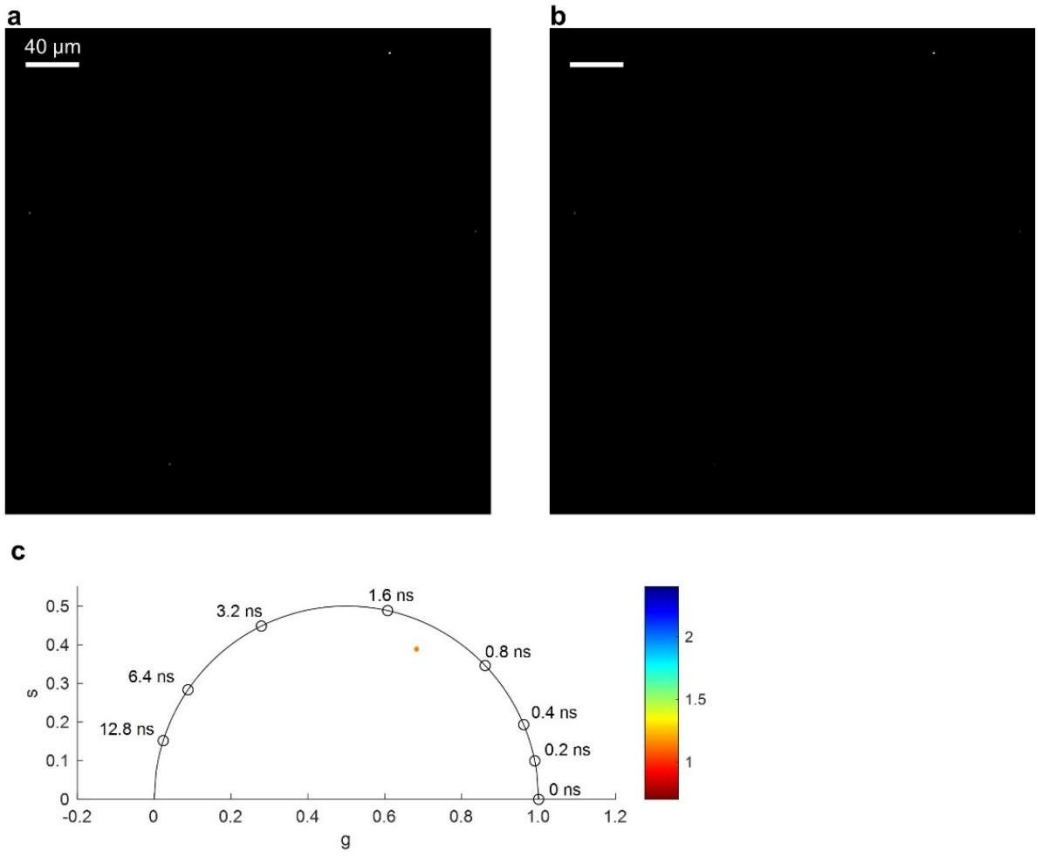

Figure 3.2. Fluorescence lifetime imaging microscopy (FLIM) of particles isolated from unused media [46]. (a) NAD(P)H intensity after segmentation; comparable with the extracellular vesicle (EV) NAD(P)H intensity in **Figure 2.4**. (b) Fluorescence lifetime-weighted intensity image; comparable with **Figure 3.1(a)**. Fluorescence lifetime values in ns are given by the color bar in (c) in ns; scale bars represent 40 µm. (c) Phasor plot of fluorescence lifetime profiles present in unused media; comparable with **Figure 3.1(d)**. Fluorescence lifetime values and color bar given in ns.

3.4 Repeatability

FLIM measurements were performed with freshly isolated EVs from MDA-MB-231 cells imaged two passages (one week) apart. At passage #10, the imaged EVs had a mean ± standard deviation NAD(P)H fluorescence lifetime of 1.57 $\pm$ 0.28 ns (**Figure 3.3(a)**). Likewise, at passage #12, the images EVs had a mean ± standard deviation NAD(P)H fluorescence lifetime of 1.58 $\pm$ 0.25 ns (**Figure 3.3(b)**). Gaussian distributions were fit to the histogram data (**Figure 3.3(c)**), and the two samples were found to be not significantly different ($p = 0.7588$). The phasor plots showing one dot per each EV for EVs derived from both passages are shown in **Figure**

3.3(d,e). NTA data showed that the concentration (mean ± standard error) of isolated EVs was $4.77 \pm 0.754 \times 10^8$ particles/mL for passage #10 and $2.68 \pm 0.0738 \times 10^8$ particles/mL for passage #12, and the number of visible EVs was almost 5 times lower in FLIM data for passage #12. This is likely due to a nonuniform distribution of EVs in the 2% agarose gel and pipetting error [46].

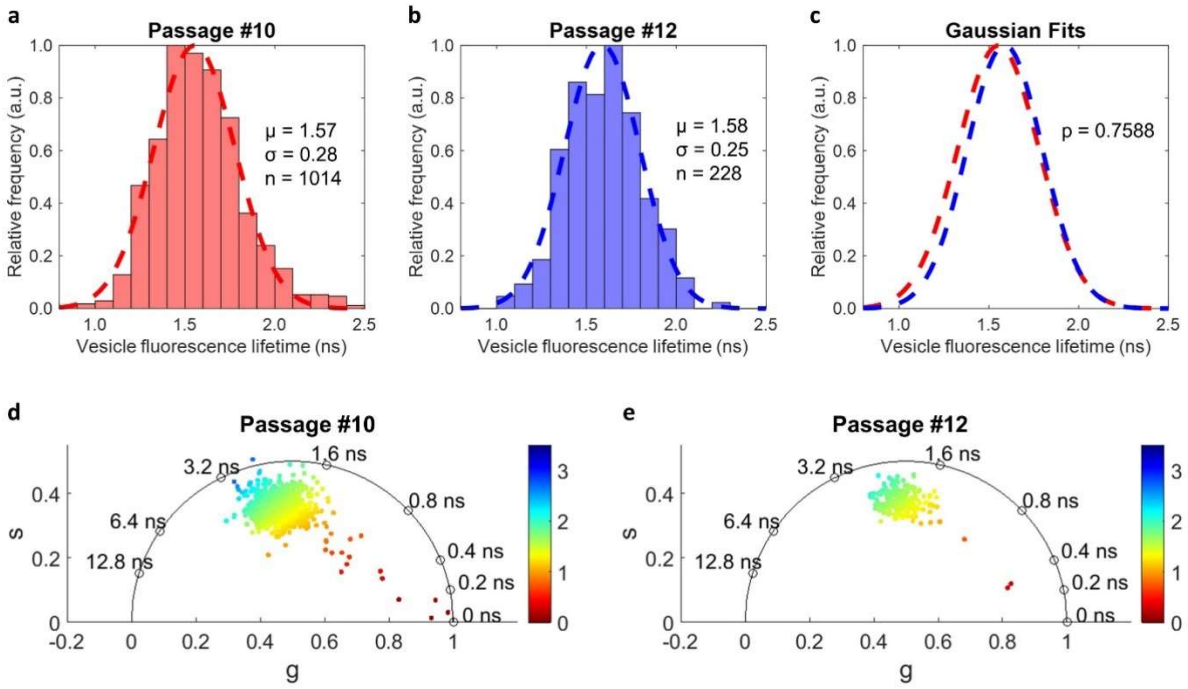

Figure 3.3. Fluorescence lifetime imaging microscopy (FLIM) profiles from two different extracellular vesicle (EV) isolations under similar conditions [46]. (a, b) Histograms of the relative number of EVs by fluorescence lifetime (*bars*) and a Gaussian fit (*dashed line*) for two different EV isolations. (c) Gaussian fits compared with a Student's t test; the two samples are not significantly different with p = 0.7588. (d, e) Phasor plots of the mean fluorescence lifetimes present in the two different samples. Color bar represents fluorescence lifetime in ns. Mean and standard deviation values given in ns; n is the number of EVs analyzed in each sample.

3.5 Human biofluid-derived EVs

As part of an ongoing study, EV isolation has been performed from human biofluid samples from patients at Carle Foundation Hospital (Urbana, IL) under a protocol approved by the Institutional Review Board (IRB) of both institutions. This study of collection and label-free detection of human biofluid EVs was approved by the Ethics Committee of University of Illinois at Urbana-Champaign (IRB protocol No. 19281) and Carle Foundation Hospital (IRB protocol No.

18CCC1708) and conducted in adherence with the Declaration of Helsinki. Urine and blood were collected from healthy or breast cancer female adult volunteers, subsequent to obtaining written informed consent. Volunteers were requested to collected samples of afternoon urine. Specimens were transported on ice from the hospital to the lab and were processed immediately. Serum was isolated from coagulated approximately 10 mL of venous blood collected from each subject in coagulant free serum separation tubes.

The purpose of this study is to determine the feasibility of characterizing human-derived EVs from blood serum and urine and the relationship between optical properties of EVs and breast cancer status. It has previously been shown that EVs can be isolated from these fluids [18], but no autofluorescence microscopy has been performed on human biofluid-derived EVs. The presented EVs were isolated from urine and blood samples from one volunteer who is a breast cancer patient. Samples were isolated with the same differential ultracentrifugation procedure as the cell culture fluid. The provided data below in **Figure 3.4** shows initial promise that FLIM of NAD(P)H can be used to image and characterize EVs derived from human urine (**Figure 3.4a,c**) and serum (**Figure 3.4b,d**), and that urine-derived EVs from this patient had a much lower NAD(P)H fluorescence lifetime ($p < 0.001$) than serum-derived EVs (**Figure 3.4e)**.

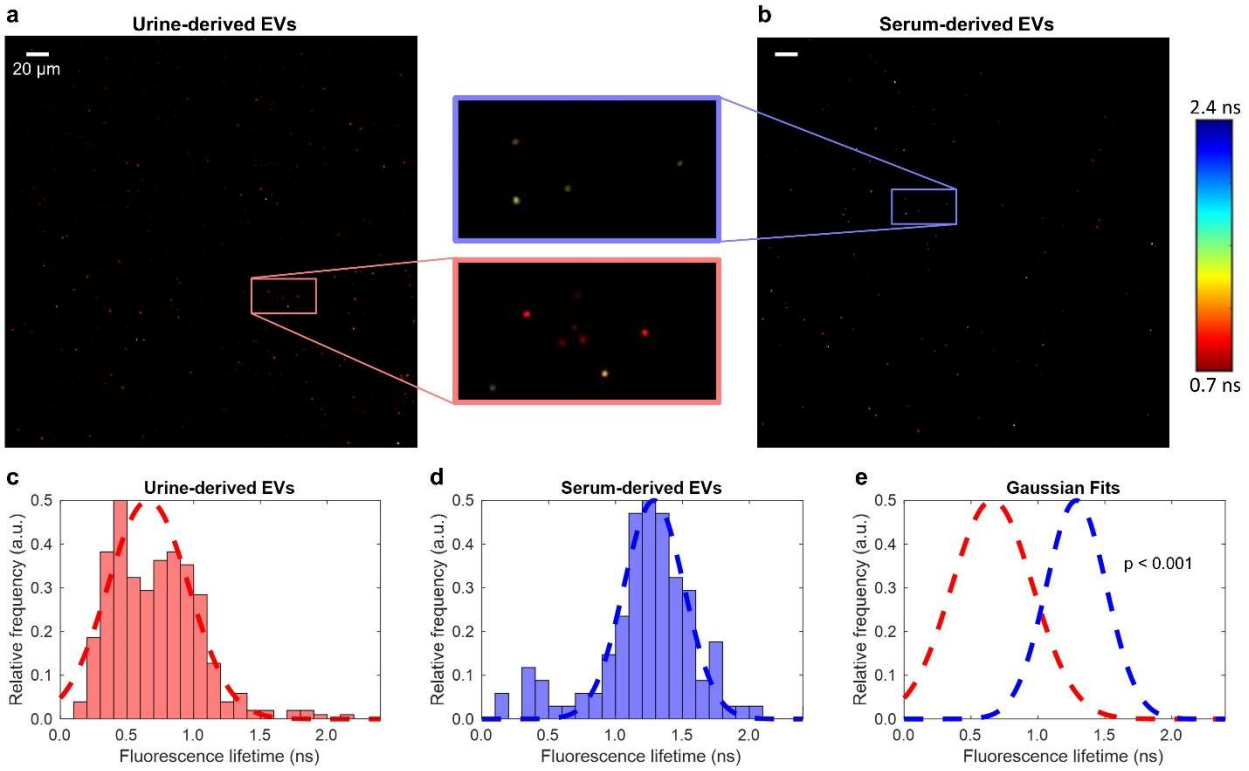

Figure 3.4: Extracellular vesicles (EVs) derived from human urine and serum. The lifetime-weighted images show the intensity and mean fluorescence lifetime of EVs isolated from (a) human urine and (b) human serum. Color bar represents fluorescence lifetime in ns; scale bars represent 20 µm. Histograms of the relative number of EVs by fluorescence lifetime (*bars*) and a Gaussian fit (*dashed line*) for (c) urine- and (d) serum-derived EVs. (d) Gaussian fits from the EVs derived from urine (*red*) and serum (*blue*) compared with a Student's t test; the two samples are significantly different with $p < 0.001$.

3.6 Discussion

The presented data show that FLIM can be used to image and characterize NAD(P)H autofluorescence originating from single EVs derived from cell culture media, human urine, and human serum. Single EV analysis suggests that EV samples derived from MDA-MB-231 cells (**Figure 3.1**), human urine (**Figure 3.4a**), and human serum (**Figure 3.4b**) all contain EVs with a range of profiles of protein-bound and free NAD(P)H, and that very little contamination or particulates from media contribute to the imaged EVs (**Figure 3.2**). EVs with a similar NAD(P)H intensity can have different NAD(P)H fluorescence lifetime (**Figure 3.1(b,c)**), which exemplifies how fluorescence lifetime of NAD(P)H can provide complementary data to the intensity. Moving

forward, it will be important to consider these implications on NAD(P)H autofluorescence intensity and lifetime imaging of EVs, and a combined multi-modal approach using FLIM and SLAM would be beneficial for a more complete EV characterization.

For analysis of EV NAD(P)H fluorescence lifetimes, the heterogeneity and distribution of fluorescence lifetimes fit well to a Gaussian curve (**Figure 3.3(a-c)**) for samples derived from cell culture fluid. The fluorescence lifetimes present in EVs from two different isolation attempts that differed only by passage number were not significantly different (**Figure 3.3(a,b)**), which shows initial promise that FLIM of NAD(P)H in EVs is repeatable. However, in order to strengthen this conclusion, in the future it will be important to characterize the NAD(P)H fluorescence lifetimes from many more EVs derived from a variety of sources and cells lines.

The methods for analysis of cell-derived EVs were applied to EVs derived from human urine (**Figure 3.4a,c**) and serum (**Figure 3.4b,d**). The urine-derived EVs have a wider fluorescence lifetime distribution and do not fit as well as cell-derived or serum-derived EVs to the Gaussian curve. As this study continues, data from many more subjects will be collected and analyzed, which will determine if the observed patterns from this single subject are a universal trend. The future data will also provide information to evaluate the clinical significance of NAD(P)H fluorescence lifetime of biofluid-derived EVs.

4. FUNCTIONAL CHARACTERIZATION OF EXTRACELLULAR VESICLES

4.1. Motivation: functional analysis of EVs

As previously stated, there is no widespread accepted technology to examine the functional properties of EVs, and evidence suggests that FLIM and other nonlinear optical techniques could provide that. The effect of storage duration and storage conditions on EVs is also not fully characterized, and is hypothesized to change their functional properties and activity [65]. Storage at -80°C is generally considered to have the most mild effect on EVs, however more data is needed to fully characterize this phenomenon [65]. Examining the effect of storage on EVs can provide an assessment on the ability of FLIM to provide a characterization of EV state and integrity with single EV resolution.

One previous study to characterize EV functionality examined EVs with antibacterial properties, and measured how those properties changed with storage [66]. Their results showed that storage at +20°C, +4°C, and -20°C significantly decreased the antibacterial effect of EVs after storage. However, storage at -80°C for up to 28 days did not significantly change the antibacterial effects, though the antibacterial effects did tend to decrease over time [66].

Another means of examining EV function is to examine their effect on macrophages. Macrophages are immune cells that uptake and destroy harmful particles such as bacteria to protect the body. Previous studies have examined the effect of EVs on macrophages, and found that macrophages uptake and react to EVs [67,68]. One study showed that the release of nitric oxide (NO) by macrophages was dependent on the dose of EVs that was applied to macrophages [67]. They also showed that this response changed when EVs from different sources were used, and that macrophages stimulated with EVs exhibited enhanced phagocytosis [67]. Another study showed

that glioblastoma-derived EVs transferred miRNA to microglia and macrophages in the brain *in vivo* using multiphoton microscopy and fluorescence tags [68]. These findings support the hypothesis that EVs functional properties of EVs can be examined via their effect on other cells such as macrophages, though this type of experiment does not allow for single EV analysis. Furthermore, previous work studying FLIM of NAD(P)H in cells has shown that the NAD(P)H fluorescence lifetime profile of macrophages that are chemically activated is different than those of untreated macrophages [69].

Through examining the effect of storage on EV NAD(P)H fluorescence lifetime, and the effect of EVs on macrophages, this research should elucidate more information about how storage affects the properties of EVs, and examine how EV functional properties can be measured using FLIM.

4.2. Storage of EVs

4.2.1. Melanoma (B16F10) cell-derived EVs

EVs were isolated from melanoma cells with the previously described procedure, and then imaged after storage under one of three conditions: 1) fresh, 2) stored in a refrigerator at 4°C, or 3) stored in a freezer at -20°C. On the indicated day, after up to a week of storage, samples were removed from storage and immediately plated in agarose gel and imaged. Some samples were contaminated or could not be imaged for logistical reasons, and were excluded from the presented data. The mean fluorescence lifetime ± the standard deviation is shown below in **Figure 4.1** for three isolation replicates of the same procedure. Of the stored samples, 11/14 had significantly different fluorescence lifetime profiles than the original fresh samples.

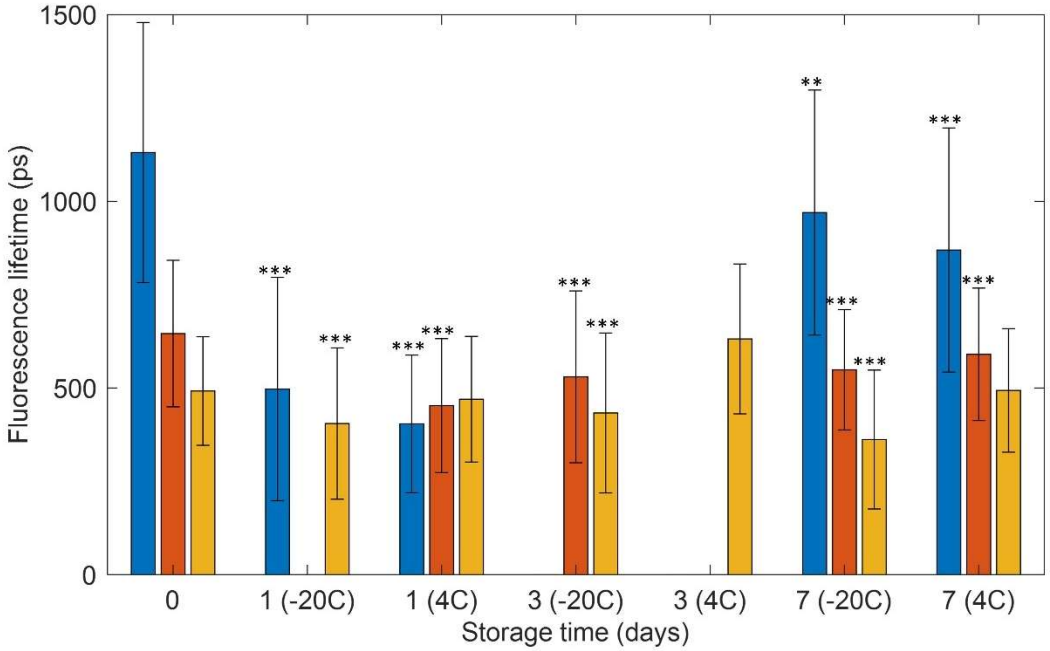

Figure 4.1: Effect of storage on the NAD(P)H fluorescence lifetime of mouse melanoma cell culture derived extracellular vesicles (EVs). Three replicates are indicated by the three colors. Each color represents EVs isolated in the same batch. ** indicates $p < 0.01$, *** indicates $p < 0.001$ from Day 0.

After examination of **Figure 4.1**, one may note that the fresh samples all appear very different, which is concerning. After further examination of B16F10-derived EVs, it was hypothesized that the large low lifetime component is due to melanin contamination, which could also be seen with the naked eye as black spots in the isolated EV sample. This calls into question the validity of the data presented in **Figure 4.1**, which resulted in the experiment being repeated in other cell lines.

4.2.2. Breast cancer (MDA-MB-231) and glioblastoma (U87) cell-derived EVs

The previously mentioned isolation procedure was used on human breast cancer MDA-MB-231 cells and human glioblastoma U87 cells. Immediately after isolation, samples were stored in -80°C for a given amount of days, up to two weeks, though one isolation yielded enough for an extra sample to be frozen and examined after 90 days in storage. Similar to the previous storage experiment, sufficient data was not able to be collected on each day due to contamination and

logistical issues. It will be important for future researchers to process data as soon as possible after EV imaging to ensure the initial data does not look contaminated, such as with particles too large and bright to be EVs. The resulting fluorescence lifetime for a given amount of time in storage at -80°C for the two cell lines is shown in **Figure 4.2**.

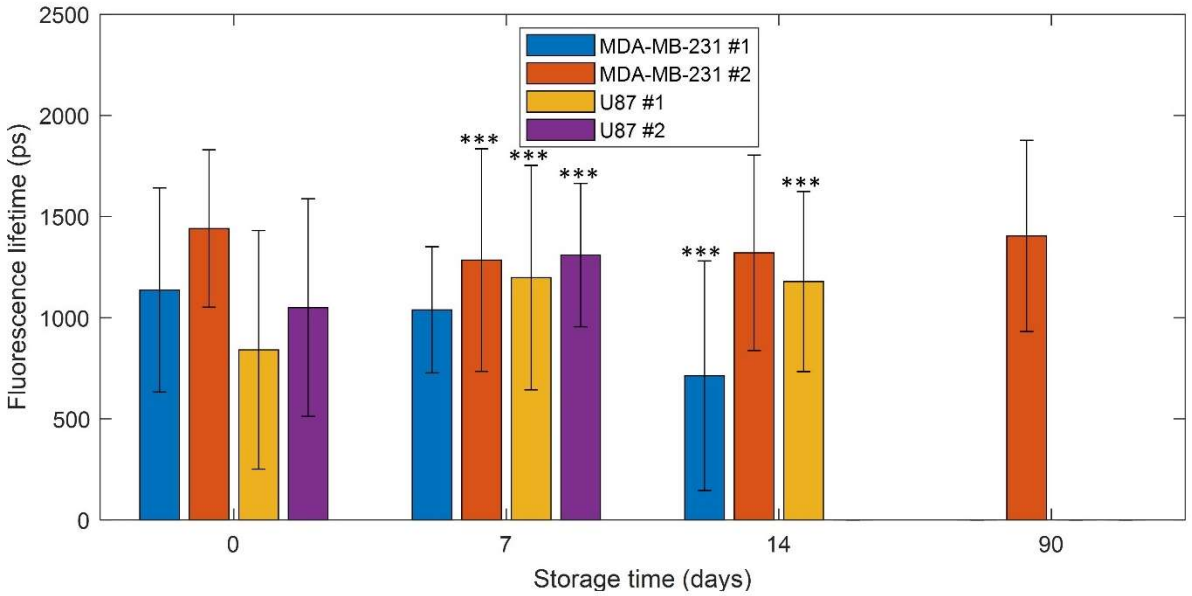

Figure 4.2. Fluorescence lifetime profiles of fresh extracellular vesicles (EVs) and EVs stored at -80°C. Each color represents EVs isolated in the same batch. Significance was determined using a student's t test, *** indicates $p < 0.001$.

The results in **Figure 4.2** show that 63% (5/8) of stored samples were significantly different that the fresh sample; however they show no clear trend between storage time and fluorescence lifetime, with some samples having longer mean fluorescence lifetime than the fresh samples and others having shorter fluorescence lifetimes.

4.3. Effect of EVs on Macrophages

Macrophages were plated on coverslips, imaged, and then either left untreated, treated with MDA-MB-231 derived EVs, or treated with a known substance to affect the macrophage response. Lipopolysaccharides (LPS) and interferon-γ (IFN γ) were used in combination to polarize the macrophages and bring about a pro-inflammatory response, and phorbol myristate acetate (PMA)

was used to activate macrophages. After 24 hours, macrophages from each group were imaged with FLIM; three dishes were untreated, three dishes were treated with 20 µL of freshly isolated EVs from MDA-MB-231 cells, and one dish each were treated with LPS + IFNγ and PMA. The amount of MDA-MB-231 derived EVs applied to the macrophages would correspond with the amount of EVs present in 20 mL of cell culture fluid, which is 10 times larger than the volume of the imaging dishes. Fluorescence-lifetime weighted images, with representative images from each dish, are shown below in **Figure 4.3**. It appears that after 24 hours in culture, and potentially due to being taken out of the incubator for imaging, the untreated group resulted in a higher fluorescence lifetime than the pre-treatment group.

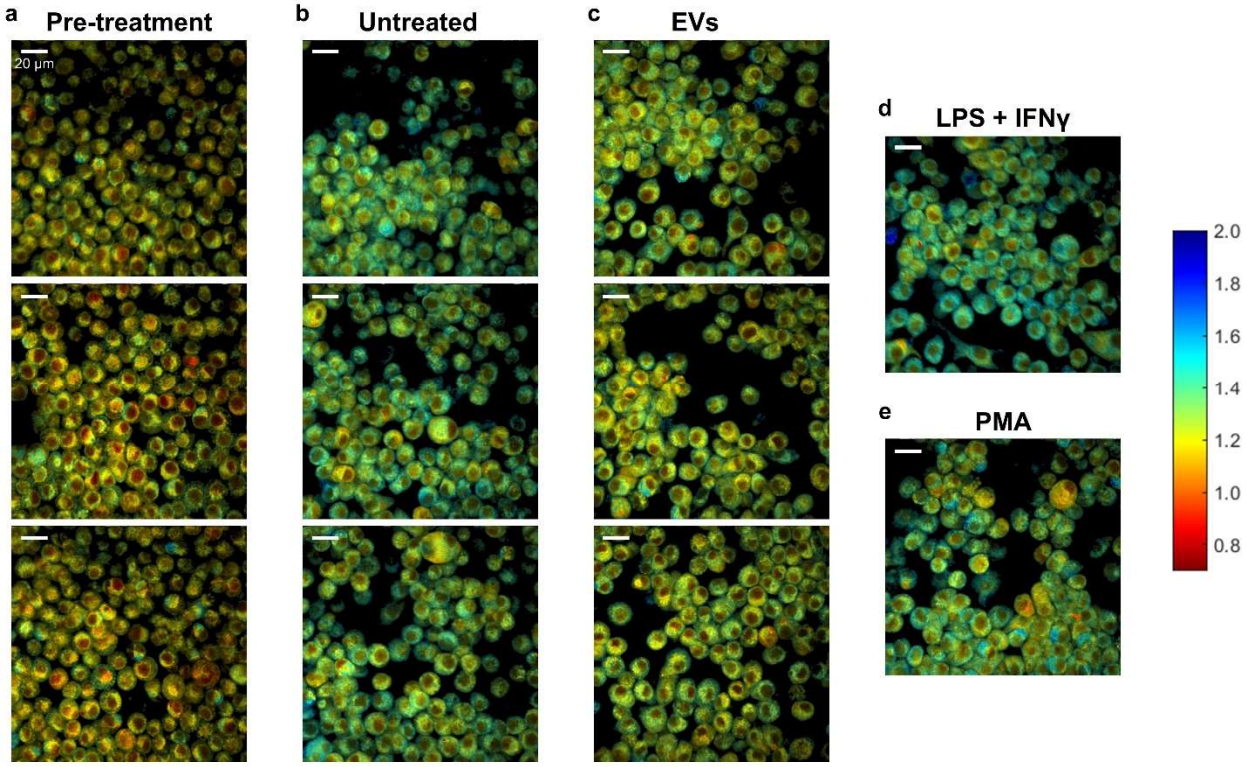

Figure 4.3: Macrophage NAD(P)H fluorescence lifetime weighted images before and after treatment. Test groups include: (a) pre-treatment, and 24 hours post-treatment with (b) nothing, (c) extracellular vesicles (EVs), (d) Lipopolysaccharides (LPS) and interferon-γ (IFN γ), and (e) phorbol myristate acetate (PMA). Color bar indicates fluorescence lifetime in ns.

Four images total were taken of each dish, and the phasor decomposition of all images per dish are combined and are shown in **Figure 4.4**.

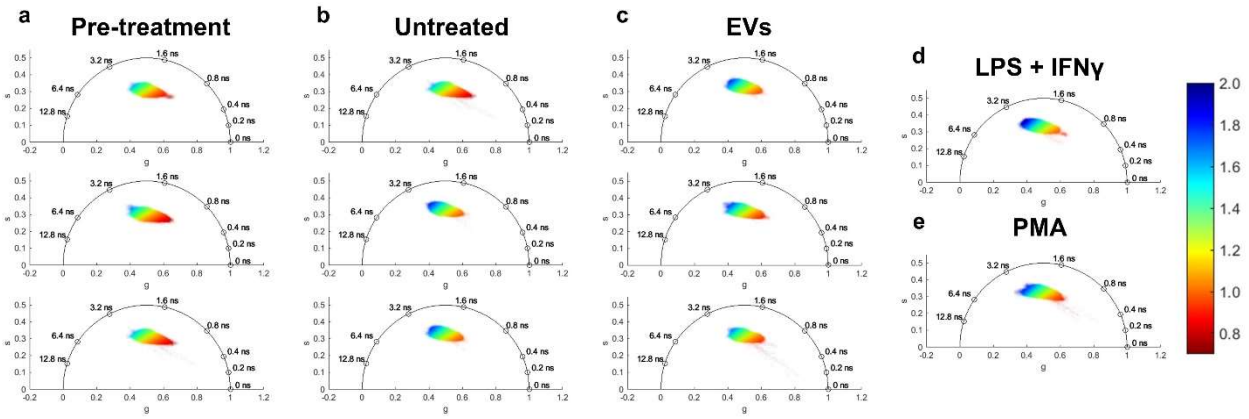

Figure 4.4: Phasor analysis of macrophage NAD(P)H fluorescence lifetime response to treatment. Test groups include: (a) pre-treatment, and 24 hours post-treatment with (b) nothing, (c) extracellular vesicles (EVs), (d) Lipopolysaccharides (LPS) and interferon-γ (IFN γ), and (e) phorbol myristate acetate (PMA). Color bar indicates fluorescence lifetime in ns.

Further analysis was done and the mean ± standard deviation of pixel fluorescence lifetime is given in **Figure 4.5** below. All groups were found to be significantly different ($p < 0.001$) than the other groups with a Student's t test.

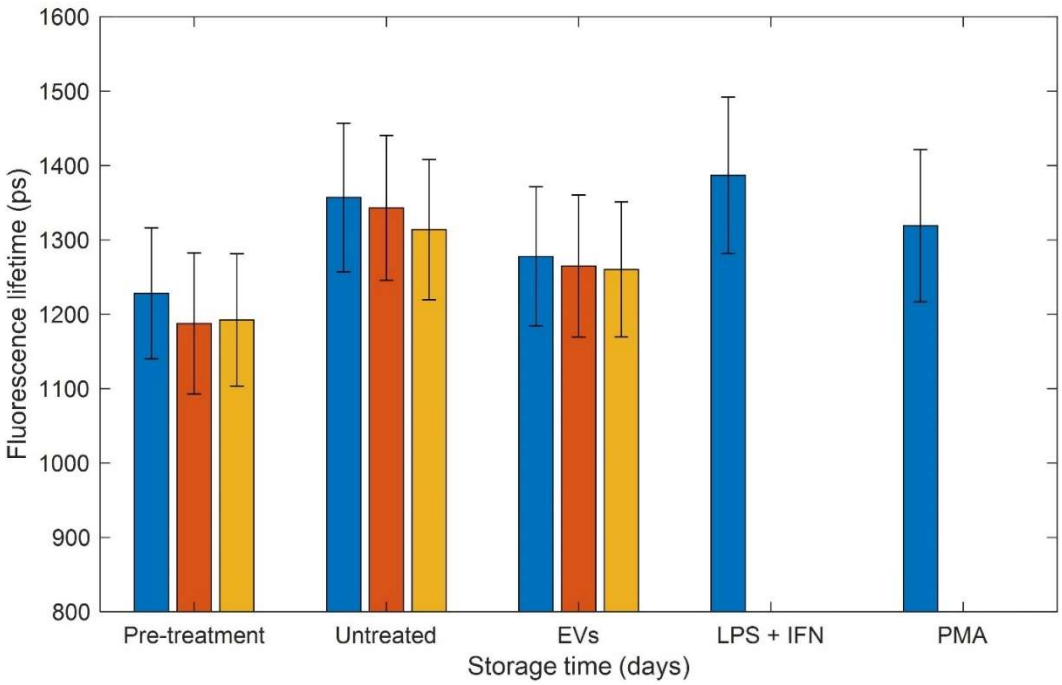

Figure 4.5:Bar chart of fluorescence lifetimes of macrophages before and after treatment. Each bar represents four images of one dish; multiple bars for the first three groups indicated that those groups had 3 dishes. Test groups include: pre-treatment, and 24 hours post-treatment with nothing (untreated), extracellular vesicles (EVs), Lipopolysaccharides (LPS) and interferon-γ (IFN γ), and phorbol myristate acetate (PMA). Error bars represent standard deviation.

4.4. Discussion

The results presented in **Section 4.2** indicate that there is often a significant difference in the fluorescence lifetime distribution of fresh and stored EVs (**Figure 4.1**, **Figure 4.2**), however a clear trend towards higher or lower fluorescence lifetimes after storage cannot be established at this time. These initial results warrant repeating, along with further investigation into the functional changes in EVs that can be induced with storage and imaged with FLIM. It is also interesting to note that even after 90 days in storage, one sample retained very similar fluorescence lifetime values to the fresh sample, indicating there may not be a progressive decline and deterioration that occurs as a function of time. It will be important to collect more data to better examine these results and determine how NAD(P)H in EVs changes with storage.

Initial data in **Figure 4.3**, **Figure 4.4**, and **Figure 4.5** suggest that EVs can elicit a metabolic response in macrophages that is observable with FLIM. Previous work showed that macrophages exhibiting a pro-inflammatory response (stimulated with LPS + IFNγ) have a shorter fluorescence lifetime than untreated, and that macrophages exhibiting a pro-healing response (stimulated with IL-4 and IL-13) show an increased fluorescence lifetime [69]. However, with only one dish tested, the presented results in **Figure 4.5** shows an increase in fluorescence lifetime in response to LPS + IFNγ. Future work is needed for better characterization and clarification, but this initial data suggests that monitoring the effect of EVs on macrophages could help to characterize the functionality of EVs.

5. RELATIONSHIP BETWEEN EXTRACELLULAR VESICLES AND PARENT CELLS

5.1. Motivation: EVs as biomarkers of disease

Researchers have suggested EVs are attractive biomarkers for cancer, including for liquid biopsy, since biofluids such as urine and serum are easily collected from patients and contain EVs [6]. Considering a liquid biopsy from a patient with a tumor, circulating EVs will originate from both the tumor and from healthy tissue. In order to separate these healthy and cancer-associated subpopulations, single EV characterization that can link EVs to their parent cells and environments is needed. FLIM of NAD(P)H is often used to characterize changes in cellular metabolism [41], so the ability to distinguish EVs derived from cells grown under different metabolic conditions was tested [46].

5.2. Metabolic perturbations of cells

To explore the effect of parent cell metabolism on EV NAD(P)H fluorescence lifetime, MDA-MB-231 cells were incubated for 48 hours in DMEM with or without 25 mM glucose prior to EV isolation; standard DMEM has 25 mM glucose. The experiment was repeated twice and the data from both sets was pooled together. Histograms and Gaussian fits of the fluorescence lifetime values of EVs from the two conditions are shown in **Figure 5.1(a-c)**. The EVs isolated from the glucose-deprived cells had significantly longer NAD(P)H fluorescence lifetimes ($p < 0.001$) compared to the EVs isolated from the cells incubated in media with glucose; mean and standard deviation fluorescence lifetime values are represented in **Figure 5.1(d)**. The phasor plot in **Figure 5.1(e)** shows that more of the glucose-deprived EVs (*blue*) are closer to the longer fluorescence lifetime components indicative of protein-bound NADPH compared to the control EVs (*red*) [46].

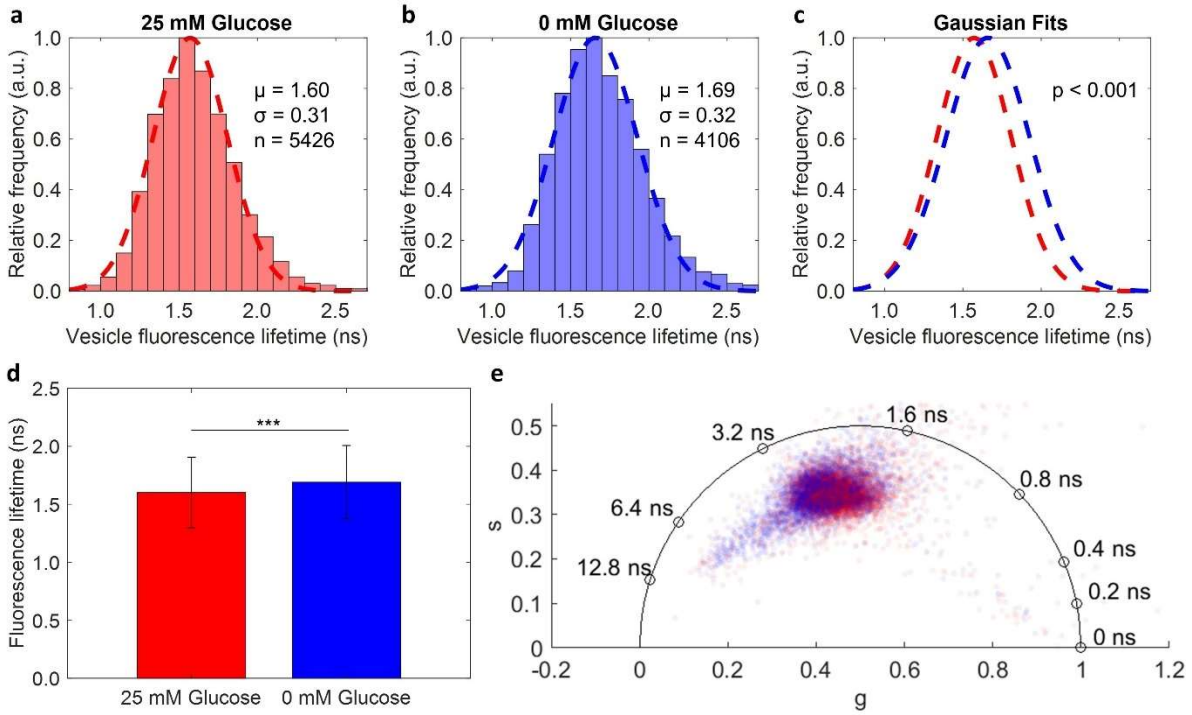

Figure 5.1. Effect of parent cell glucose deprivation on the fluorescence lifetime of cell-derived extracellular vesicles (EVs) [46]. (a, b) Histograms of the relative number of EVs by fluorescence lifetime (*bars*) and a Gaussian fit (*dashed line*) for (a) 25 mM glucose and (b) 0 mM glucose. (c) Gaussian fits from 25mM glucose (*red*) and 0 mM glucose (*blue*) samples compared with a Student's t test; the two samples are significantly different with $p < 0.001$. (d) Bar graph showing mean and standard deviation of EV fluorescence lifetime. (e) Phasor plots showing the 2D distribution of lifetime components for the two samples. *** indicates $p < 0.001$. Mean and standard deviation values given in ns; n is the number of EVs analyzed in each sample.

5.3. EVs and spatial analysis of cells

FLIM of NAD(P)H was also used to compare the metabolic state of parent cells and the EVs they produced. MDA-MB-231 cells were plated 48 hours prior to imaging and serum-starved for 24 hours prior to imaging to mimic the state of cells when they are producing EVs for analysis. As shown in **Figure 5.2**, the fluorescence lifetimes present in EVs is longer and wider than the distribution of fluorescence lifetimes present in pixels regions from cells imaged using the same parameters. The two fluorescence lifetime distributions were found to be significantly different using a Student's t test ($p < 0.001$) [46].

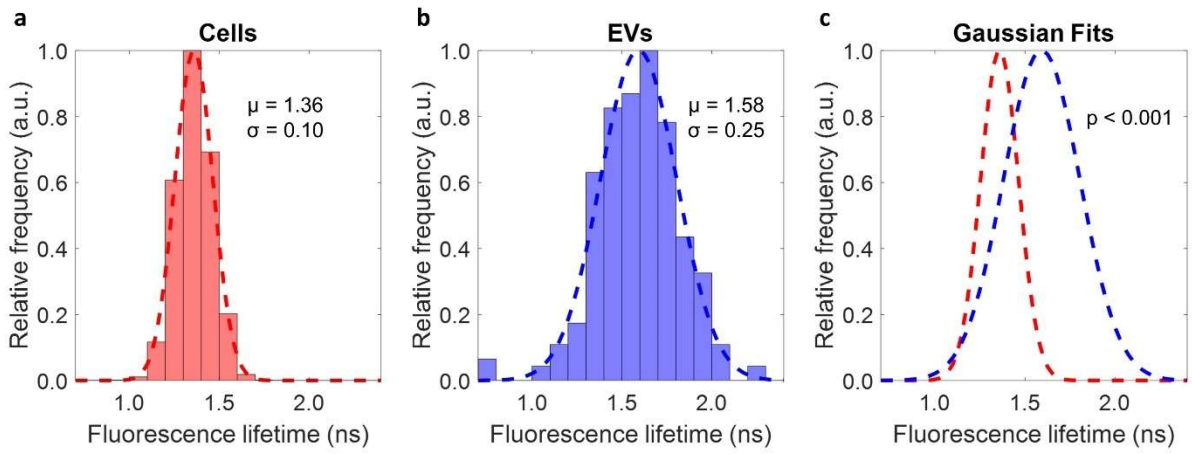

Figure 5.2. Mean fluorescence lifetime distribution of extracellular vesicles (EVs) and their parent MDA-MB-231 cells [46]. (a) Histograms of the relative number of cellular pixels by fluorescence lifetime (*bars*) and a Gaussian fit (*dashed line*). (b) Histograms of the relative number of EVs by fluorescence lifetime (*bars*) and a Gaussian fit (*dashed line*). (c) Gaussian fits of the fluorescence lifetime distribution of cells (*red*) and EVs (*blue*) compared with a Student's t test; the two distributions are significantly different with $p < 0.001$.

In order to provide a more comprehensive analysis, the fluorescence lifetime distribution of pixels in the cells was separated by manual segmentation into three major cellular components: nuclei, mitochondria, and cytosol. Examples of these cellular components are indicated with arrows on **Figure 5.3(a)**, which shows a fluorescence lifetime weighted image of the MDA-MB-231 cells. For visual comparison, a fluorescence lifetime weighted image of the EVs derived from the cells is presented as well in **Figure 5.3(b)**. Gaussian distributions (mean ± standard deviation) were fit to the fluorescence lifetime histograms of each cellular component; the nuclei (1.22 ± 0.07 ns), mitochondria (1.31 ± 0.07 ns), and cytosol (1.38 ± 0.10 ns) all had a shorter and more narrow fluorescence lifetime distributions than the EVs (1.57 ± 0.27 ns), and were all significantly different than the EV fluorescence lifetimes using a Student's t test ($p < 0.001$), as shown in **Figure 5.3(c-d)**. The fluorescence lifetime profiles of each cellular component and EVs were plotted on a phasor plot, as shown in **Figure 5.3(e)**. This plot displays the wider range of fluorescence lifetimes

present in EVs, which shows very little fluorescence lifetime profile overlap with nuclei and mitochondria, and some overlap with the cytosol [46].

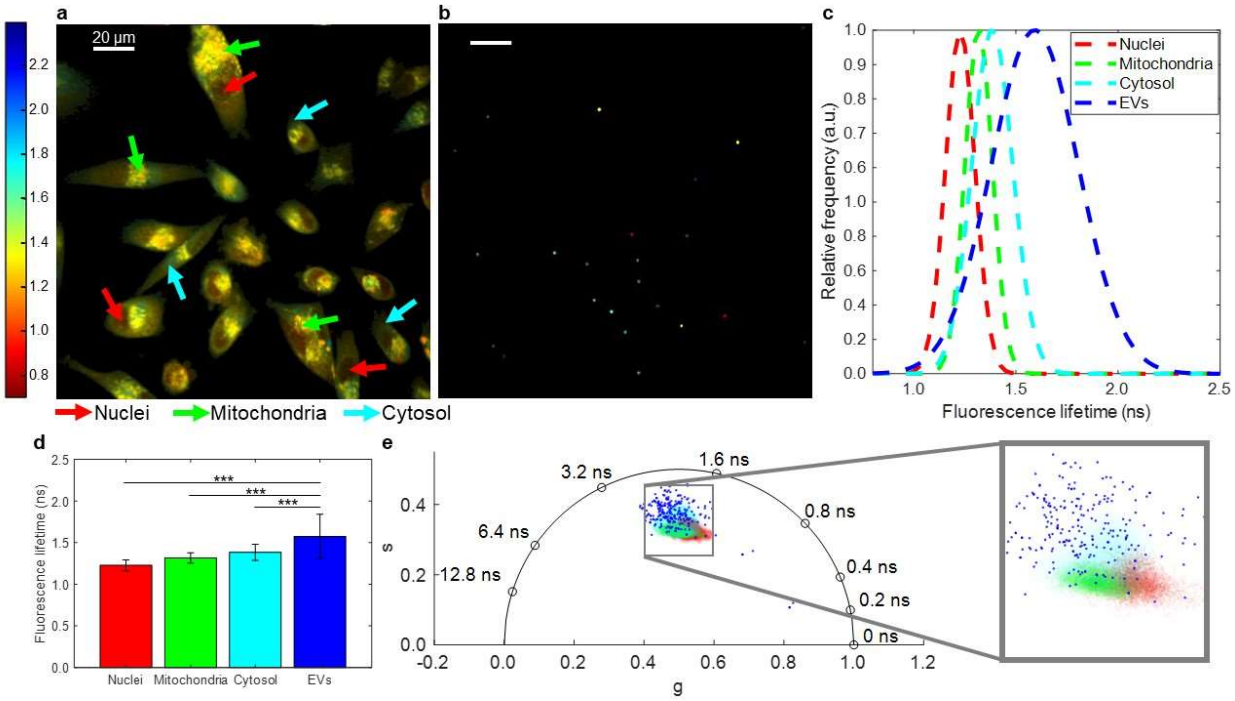

Figure 5.3. Fluorescence lifetime imaging microscopy **(**FLIM) signature of extracellular vesicles (EVs) and the main cellular components of their parent cells [46]. (a) Fluorescence lifetime-weighted image of MDA-MB-231 cells with corresponding annotation arrows for nuclei (*red*), mitochondria (*green*), and cytosol (*cyan*). (b) Fluorescence lifetime-weighted image of EVs. Color bar for FLIM images given in ns next to panel (a). Scale bars represent 20 µm. (c) Fluorescence lifetime Gaussian fits for nuclei (*red*), mitochondria (*green*), cytosol (*cyan*), and EVs (*blue*). (d) Bar chart showing mean and standard deviation of fluorescence lifetime distributions. *** indicates $p < 0.001$. (e) Phasor plot showing the phasor components of EVs (*blue*) and the cellular nuclei (*red*), mitochondria (*green*), and cytosol (*cyan*) with a zoomed in region of interest.

5.4. Discussion

FLIM of NAD(P)H has been used to study cancerous cells and tissues due to their altered metabolic function, such as the shift toward cytosolic aerobic glycolysis [42,53,56], but the application of FLIM to cell-derived EV characterization presents a new opportunity for discovery. This demonstrates that FLIM of NAD(P)H is a suitable technique for differentiating EVs from MDA-MB-231 cells maintained under different metabolic conditions, showing that cellular metabolism can cause changes in EV composition. **Figure 5.1** shows that EVs derived from

glucose-deprived MDA-MB-231 cells have a significantly longer fluorescence lifetime ($p < 0.001$) than those derived from cells in the presence of glucose [46]. This contributes to the evidence that EVs could be used as biomarkers of disease, since cellular metabolic changes indicative of cancer could be present in EVs, as suggested by previous work using SLAM microscopy [9,37]. Moreover, it has been shown that tumor-related EVs reprogram the metabolism of cells that uptake them [23,70,71], and that malignant cells create more EVs than normal cells [72]. Many have stressed the importance of understanding the metabolic and functional role of EVs in cancer [19,73,74], and the presented data suggest that future work examining the fluorescence lifetime of NAD(P)H in EVs could eventually contribute to understanding and quantifying their metastatic potential. This will be relevant as more data is collected in the human biofluid study mentioned in **Section 3.5**. EVs from patients with and without breast cancer can be compared, and perhaps the differences in EV NAD(P)H fluorescence lifetime can be linked to the metabolism and/or breast cancer status of the subject.

From the phasor plot in **Figure 5.1(e)**, it appears that the longer fluorescence lifetime of EVs derived from cells without glucose is due to a fluorescence lifetime characteristic of a longer protein-bound NAD(P)H component [46], which corresponds more to previously determined protein-bound NADPH values, rather than protein-bound NADH [40,57]. The lack of glucose stresses the cells by depriving them of their main nutrient, as discussed in **Section 1.2.1**, which can have various diverse downstream metabolic effects. Glucose was not present in the cell media, but the essential amino acid L-glutamine was. Glutamine can be metabolized in cells through conversion to glutamate and then to α-ketoglutarate (one of the intermediates in the TCA cycle) by glutamate dehydrogenase, which uses NADPH as a cofactor. This is a possible explanation for increased NADPH in glucose-deprived cells, leading to increased NADPH in the glucose-deprived

EVs. NADH is created through glycolysis, so a lack of glucose will lead to less NADH in the cells, which in turn may lead to less NADH in the EVs. These two factors put together could account for a relatively longer protein-bound fluorescence lifetime component in EVs derived from glucose-deprived cells since these mechanisms would lead to a higher NADPH:NADH ratio [46]. It has also been hypothesized that senescent cells output EVs with more NADPH related to the pentose phosphate pathway [61], and it is possible that the cellular stress from lack of glucose puts the cells in a similar state. Although future work is needed to examine the hypothesized connection between the EV proteomic and metabolite profile and its fluorescence lifetime, our results show that the NAD(P)H fluorescence lifetime of EVs may be related to the metabolic state of the parent cells.

To take advantage of the fact that FLIM is well-established for use in live cell imaging, MDA-MB-231 cells were plated and imaged under the same imaging parameters as their corresponding EVs, as shown in **Figure 5.3(a, b)**. The fluorescence lifetime distributions of the cells and EVs were found to be significantly different (**Figure 5.2**). However, the fluorescence lifetime profile of the EVs has partial overlap with the cellular fluorescence lifetime profiles on the phasor plot (**Figure 5.3(e)**), which indicates that a subpopulation of EVs have similar protein-bound and free NAD(P)H fluorescence lifetime profiles when compared to some areas of cells [46]. The NAD(P)H autofluorescence in cells is generally assumed to be primarily NADH, since there is about 10 times more NAD+/NADH in cells than NADP/NADPH [49]. This implies that the subpopulation of the EVs that overlap with the cells on the phasor plot also have a FLIM signature dominated by NADH. Furthermore, although the fluorescence lifetime values of the EVs are significantly different from those of the main cellular components, they have the most overlap

with the values associated with the cytosol, rather than the nuclei or mitochondria of live cells (**Figure 5.3(c-d)**).

Figure 5.3(e) shows that almost no EVs have similar fluorescence lifetime profiles to the nucleus, a few have similar profiles to the mitochondria, and many overlap with the more broad profile of the cytosol [46]. The majority of EVs tend to contain a more prominent protein-bound NAD(P)H component than the cells. Previous proteomic studies suggest that the makeup of EVs is closely related to that of the cytosol and plasma membrane, and less likely to be similar in composition to the cell nucleus or mitochondria [19,21,22,75]. Furthermore, proteins are enriched in EVs when compared to cells, some of which can have up to 100x higher concentration in EVs than in cell lysate [7]. This protein enrichment in EVs could explain the subpopulation of EVs with a longer fluorescence lifetime than the cytosol due to more protein-bound NAD(P)H; whereas the other subpopulation may be a sampling of the parent cell cytosol. Additional studies are required to clarify whether this EV fluorescence lifetime profile indicative of a protein enriched cytosol is a unique feature of the MDA-MB-231 cell line or the same is found in other types of cells and tissues.

Proteomic studies have shown a high number of proteins present in EVs are involved in cellular metabolism and the antioxidant response, some of which use NADH or NADPH as cofactors or substrates [21,23,61,73,75-85]. An incomplete list of these proteins is given in **Table 5.1** [46]. Notably, glyceraldehyde-3-phosphate dehydrogenase (GAPDH), a cytosolic enzyme involved in glycolysis that uses NADH as a cofactor (**Figure 1.1**), is one of the most commonly identified proteins in EVs [21,76]. Isocitrate dehydrogenase (IDH1, IDH2) has been identified in EVs [61,77,78], and nucleic acid studies have found both mutated mRNA for IDH1 [73] and miRNA that downregulates IDH1 and IDH2 activity has been found in breast cancer EVs [23].

Table 5.1: Gene names, NADH or NADPH affiliation, primary cellular location, and references containing evidence for various proteins found in EVs [46]. All cited studies used mass spectrometry for protein identification unless indicated with * for Western Blot or + for flow cytometry.

Gene name	NADH or NADPH	Primary cellular location	References
GAPDH	NADH	cytosol	32, 61, 75, 77-82
LDHA	NADH	cytosol	61, 75, 79, 80, 81
LDHB	NADH	cytosol	61, 77, 79
LDHC	NADH	cytosol	79
PHGDH	NADH	cytosol	61
MDH1	NADH	cytosol	32, 61, 80
HPGD	NADH	cytosol	78
CYB5R1	NADH	cytosol	78
ADH1A	NADH	plasma membrane	77, 80
ADH1B	NADH	plasma membrane	77, 80
PDHA	NADH	mitochondria	61, 79
PDHB	NADH	mitochondria	61
ALDH 7A1	NADH	mitochondria	61
Q9NX14	NADH	mitochondria	79
ALDH6A1	NADH	mitochondria	77
G6PD	NADPH	cytosol	61, 75, 77
PGD	NADPH	cytosol	61*, 75, 77, 78
GRHPR	NADPH	cytosol	61
AKR1A1	NADPH	cytosol	78, 79
IDH1	NADPH	cytosol	61, 75, 77, 78
IDH2	NADPH	cytosol	61, 77
BLVRB	NADPH	cytosol	61, 75, 78
ALDH1L1	NADPH	cytosol	80
GLUD1	NADPH	mitochondria	61, 77
DHRS2	NADPH	mitochondria	80
AKR1D1	NADPH	nucleus	80
CBR1	NADPH	nucleus	75, 78
POR	NADPH	nucleus	80
NQO1	NADPH, NADH	cytosol	61, 75, 77
CD38	NADPH, NADH	plasma membrane	83*, 84+
CD157	NADPH, NADH	plasma membrane	84+

In addition to their roles as cofactors for metabolic enzymes, NAD+/NADH and NADP/NADPH can also act as signaling molecules or as substrates for other biochemical pathways [49,84,86]. For example, NAD+ is a substrate for cyclic ADP-ribose (cADPR) synthases

CD38 and CD157 [84,86], both of which have been found to be over-expressed in EVs originating from the bone marrow of patients with multiple myeloma, when compared with control patients [84]. Moreover, CD38 has also been found to be enzymatically active in EVs derived from human lymphoblastoid B cells and is hypothesized to be a key intracellular messenger [83]. Though there is still much to learn about the biochemical makeup and functions of EVs, we know that they contain a variety of NAD(P)H related enzymes, and the presented FLIM data has confirmed a diverse profile of protein-bound NAD(P)H within EVs. Thus, a diverse profile of protein-bound NAD(P)H in EVs is expected. Future work with FLIM is needed to determine how the up- or down- regulation of specific proteins in cells and EVs alters the fluorescence lifetime profile. Note that many of the proteins mentioned above and in **Table 5.1** also appear in **Figure 1.3**, which describes pathways in cellular metabolism and the fates of glucose.

Many previous studies on EVs, such as those referenced in **Table 5.1**, have focused on enzymes related to NADPH and NADH without quantifying or characterizing the corresponding cofactors. With two-photon FLIM, NAD(P)H fluorescence lifetimes from hundreds of EVs can be measured within minutes, which conveys information about the NAD(P)H in EVs and the parent cells. This again supports the idea that FLIM of EV NAD(P)H could be used for examining and optically characterizing liquid biopsy specimens with high throughput.

6. CONCLUSIONS AND FUTURE WORK

6.1. Conclusions

These presented results demonstrate that FLIM offers label-free possibilities for visualizing and EVs and their spatial information, in addition to that of their corresponding cells. By combining previously determined methods for EV isolation with NAD(P)H FLIM imaging, and creating new procedures for sample embedding and image processing, FLIM can be used to characterize the NAD(P)H content of EVs. The EVs produced by MDA-MB-231 cells are heterogeneous and follow a broad Gaussian distribution of fluorescence lifetimes of NAD(P)H, with initial results suggesting this characterization is both repeatable and also possible on human-derived samples.

The ability of FLIM of NAD(P)H to examine storage-induced changes in EVs was explored, with initial results suggesting that some changes occur with storage and can be measured using FLIM. Furthermore, the idea of measuring EV functionality by monitoring the fluorescence lifetime of macrophages treated with EVs is presented. Fluorescence lifetime was also used to differentiate between EVs secreted by cells with or without glucose present in the cell culture media. EVs showed a significantly different fluorescence lifetime profile than their parent cells. The fluorescence lifetime profiles of EVs were most similar to the cell cytosol, out of the examined cellular components, and appeared to have more bound NAD(P)H than the cell cytosol. This supports previous findings that EVs are similar in composition to parent cell cytosol but can be enriched with proteins capable of binding NAD(P)H [75]. FLIM and other label-free microscopy techniques have not yet been explored broadly for EV analysis, and these results suggest that FLIM can be used to not only probe the functionality of EVs, but also provides label-free insight on the EV parent cell metabolism with single EV resolution.

6.2. Current challenges in nonlinear optical imaging of EVs

As previously stated, EVs can be as small as 50 nm in size, however the resolution of the discussed nonlinear optical imaging techniques is limited to around 500 nm. Thus, the size of many EVs is smaller than the two-photon excitation volume and image voxel. This means when considering EV autofluorescence intensity, the intensity of an image pixel can be quantified, but the intensity distribution within the corresponding sample volume to that pixel is unknown. For example, consider two EVs with the same amount of NAD(P)H, but one of diameter 200 nm and one of diameter 50 nm. The smaller EV has an NAD(P)H concentration that is 16 time larger than the NAD(P)H concentration of the larger EV. However, since both particles are below the resolution limit, when excited by multiphoton absorption, they will each result in pixels that have the same fluorescence intensity, since the intensity is proportional to the number of fluorophore molecules within the excitation volume.

This poses an interesting challenge and the need for either normalization, which so far has been addressed by ratiometric analysis of NAD(P)H and FAD [9,37,38], or for analysis of a parameter independent of concentration, such as fluorescence lifetime. However, both methods have an inherent detection limit based on the amount and intensity of NAD(P)H in the sample. Simultaneous Rayleigh and Raman scattering has been used to determine the size of EVs while also collecting their Raman spectra, and it is possible a similar technique could be combined with autofluorescence imaging of EVs in order to better understand how the size of an EV and the concentration of NAD(P)H in EVs are related. SLAM microscopy also contains a third harmonic generation (THG) channel, which images changes in refractive index [39]. EVs can be seen in the THG channel since their lipid membrane provides contrast with the aqueous inside of EVs and EV embedding material [9]. It has been shown that the THG power can change based on the size of

μm and sub-μm polystyrene beads [87], so potentially differences in THG intensity could be used to separate EVs of varying sizes. Another important note is that SLAM data showed that only a portion of EVs are NAD(P)H-rich [9], which means there is a portion of EVs that cannot be imaged with NAD(P)H FLIM alone, suggesting that a multimodal approach may be needed to analyze all EVs in a sample.

There are also many questions in the EV field, which is constantly evolving, such as the preferred classification, validation, and isolation methods for EVs. Regarding the present work, multiple samples were excluded from analysis during this process due to contamination with bacteria or larger particles and debris. It will be very important for future work to continue to revise and improve the process of EV isolation and validation as the technology and accepted standards evolve with the field.

6.3. Future directions

The presented study shows that FLIM of NAD(P)H in EVs can be performed and used for characterization, but due to the immense variability of EVs, there are many more questions to be pursued, including repeating many of the presented experiments. Additionally, a handful of experiments that will shed more light on the capabilities of FLIM of NAD(P)H in EVs are: compare the NAD(P)H fluorescence lifetime profiles from different cell lines, perform multi-modal characterization of EVs in conjunction with SLAM and Raman microscopy, examine more metabolic perturbations of parent cells and the effect on EVs, and expand the work on the cellular response to treatment with EVs. EVs should also be collected from various biofluids such as human urine and serum and imaged with FLIM to further examine the feasibility of performing liquid biopsies with FLIM NAD(P)H analysis of EVs. Additionally, the results in **Figure 3.3** showed no significant difference of EVs two passages apart, but other variation in results suggest that passage

number could have an effect on the EV NAD(P)H content [61], and thus an effect on NAD(P)H fluorescence lifetime. These experiments are just a few of the possibilities that are open for discovery now that a technique for characterizing and imaging the NAD(P)H in EVs with FLIM has been established.

There are still underlying questions about the packaging of EVs [7], and future work using FLIM could also be used to better elucidate the process of EV release, since unlike many EV analysis methods FLIM can be done on live cells, without the need for endogenous labels. Raman microscopy can also be used for cell and tissue imaging. Initial work has compared the spatial distribution of EVs in tissue [38], though more correlative studies are needed. Raman microscopy provides useful information about the macromolecular makeup and can report on different types of molecules, unlike FLIM or SLAM. However, it lacks the functional aspect for quantifying protein activity and cellular metabolism that could be performed with NAD(P)H imaging. Both CARS and stimulated Raman scattering (SRS) microscopy have been performed in conjunction with NAD(P)H and FAD autofluorescence microscopy previously [88]. As microscopy techniques are developed for EV imaging, we move closer to filling the immense need for more *in vivo* experiments for a more comprehensive understanding of EVs [19], and also continue to push for multimodal approaches to collect as much information as possible about these mysterious particles.

7. REFERENCES

[1] Cancer facts and figures 2019. American Cancer Society; https://www.cancer.org/research/cancer-facts-statistics/all-cancer-facts-figures/cancer-facts-figures-2019.html#:~:text=Estimated%20numbers%20of%20new%20cancer,deaths%20in%20the%20United%20States.), accessed July 2020.

[2] Breast cancer basic information. U.S. Department of Health and Human Services, Centers for Disease Control and Prevention; https://www.cdc.gov/cancer/breast/, accessed June 2020.

[3] Guide to cancer early diagnosis 2017. World Health Organization; https://apps.who.int/iris/handle/10665/254500, accessed June 2020.

[4] Ginsburg O, Yip CH, Brooks A, Cabanes A, Caleffi M, Antionio J, et al. Breast cancer early detection: a phased approach to implementation. Cancer 2020; 126(S10):2379-2393.

[5] Wang HX, Gires O. Tumor-derived extracellular vesicles in breast cancer: from bench to bedside. Cancer Lett. 2019;460:54-64.

[6] Becker A, Thakur BK, Weiss JM, Kim HS, Peinado H, Lyden D. Extracellular vesicles in cancer: cell-to-cell mediators of metastasis. Cancer cell. 2016; 30(6):836-848.

[7] Doyle LM, Wang MZ, Overview of extracellular vesicles, their origin, composition, purpose, and methods for exosome isolation and analysis. Cells. 2019; 8(7):727.

[8] Hartjes TA, Mytnyk S, Jenster GW, van Steijn V, van Royen ME. Extracellular vesicle quantification and characterization: common methods and emerging approaches. Bioeng. 2019;6(9).

[9] You S, Barkalifa R, Chaney EJ, Tu H, Park J, Sorrells JE, Sun Y, Liu YZ, Yang L, Chen DZ, Marjanovic M, Sinha S, Boppart SA. Label-free visualization and characterization of extracellular vesicle in breast cancer. Proc Natl Acad Sci. 2019; 116(48):24012-24018.

[10] Gadella TWJ, Jovin TM, Clegg RM. Fluorescence lifetime imaging microscopy (FLIM): spatial resolution of microstructures on the nanosecond time scale. Biophys Chem. 1993; 48(2):221-239.

[11] Yaseen MA, Sutin J, Wu W, Fu B, Uhlirova H, Devor A, Boas DA, Sakadzic S. Fluorescence lifetime microscopy of NADH distinguishes alteration in cerebral metabolism *in vivo*. Biomed Opt Express. 2017; 8(5):2368-2385.

[12] Smith CM, Marks AD, Lieberman MA, Marks DB, Marks DB. *Marks' Basic Medical Biochemistry: A Clinical Approach*. Philadelphia: Lippincott Williams & Wilkins, 2005.

[13] Hanahan D, Weinberg RA. Hallmarks of cancer: the next generation. Cell. 2011; 144(5)L646-674.

[14] Daniher P, Banski P, Payan VL, Grasso D, Ippolito L, Sonveaux P, Porporato PE. Cancer metabolism in space and time: beyond the Warburg effect. Iochim Biophys Acta Bioenerg. 2017; 1858(8):556-572.

[15] Chaffer CL, Weinberg RA. A perspective on cancer cell metastasis. Science. 2011; 331(6024):1559-1564.

[16] Ramirez MI, Amoorim MG, Gadelha C, Milic I, Welsh JA, Freitas VM, et al. Technical challenges of working with extracellular vesicles. Nanoscale. 2018;10(3):881-906.

[17] Katsuda T, Kosaka N, Ochiya T. The roles of extracellular vesicles in cancer biology: toward the development of novel cancer biomarkers. Proteomics. 2014;14(4-5):412-425.

[18] Szatanek R, Baran J, Siedlar M, Baj-Krzyworzeka M. Isolation of extracellular vesicles: determining the correct approach (Review). Int J Mol Med. 2015; 36(7):11-17.

[19] Zaborowski MP, Balaj L, Breakfield XO, Lai CP, Extracellular vesicles: composition, biological relevance, and methods of study. Bioscience. 2015; 65(8):783-797.

[20] Van der Pol E, Boing AN, Harrison P, Sturk A, Nieuwland R. Classification, functions, and clinical relevance of extracellular vesicles. Pharmacol Rev. 2012;64(3):676-705.

[21] Thery C, Ostrowski M, Segura E. Membrane vesicles as conveyors of immune responses. Nat Rev Immunol. 2009;9(8):581-593.

[22] Vader P, Breakefield XO, Wood MJ. Extracellular vesicles: emerging targets for cancer therapy. Trends Mol Med. 2014;20(7):385-393.

[23] Fong MY, Zhou W, Liu L, Alontaga AY, Chandra m, Ashby J, et al. Breast-cancer-secreted miR-122 reprograms glucose metabolism in premetastatic niche to promote metastasis. Nat Cell Biol. 2015; 17(2):183-194.

[24] Palmieri V, Lucchetti D, Gatto I, Maiorana A, Marcantoni M, Maulucci G, Papi M, Pola R, De Spirito M, Sgambato A. Dynamic light scattering for the characterization and counting of extracellular vesicles: a powerful noninvasive tool. J Nanopart Res. 2014; 16:2583.

[25] Gardiner C, Ferreira YJ, Dragovic RA, Redman CWG, Sargent IL. Extracellular vesicle sizing and enumeration by nanoparticle tracking analysis. J Extracell Vesicles. 2013; 2(1): 19671.

[26] Rikkert LG, Nieuwland R, Terstappen LWMM, Coumans FAW. Quality of extracellular vesicle images by transmission electron microscopy is operator and protocol dependent.

[27] Skliar M, Chernyshev VS. Imaging of extracellular vesicles by atomic force microscopy. J Vis Exp. 2019; (151). DOI: 10.3791/59254.

[28] Enciso-Martinez A, Van der Pol E, Hau CM, Nieuwland R, Van Leeuwen TG, Terstappen LWMM, Otto C. Label-free identification and chemical characterization of single extracellular vesicles and lipoproteins by synchronous Rayleigh and Raman scattering. J Extracell Vesicles. 2020; 9(1): 1730134.

[29] Gualerzi A, Kooijmans SAA, Niada S, Picciolini S, Brini AT, Camussi G, Bedoni M. Raman spectroscopy as a quick tool to assess purity of extracellular vesicle preparation and predict their functionality. J Extracell Vesicles. 2019; 8(1):1568780.

[30] Gualerzi A, Niada S, Giannasi C, Picciolini S, Morasso C, Vanna R, et al. Raman spectroscopy uncovers biochemical tissue-related features of extracellular vesicles from mesenchymal stromal cells. Sci Rep. 2017; 7:9820.

[31] Kowal EJK, Ter-Ovanesyan D, Regev A, Church GM. Extracellular vesicle isolation and analysis by western blotting. Methods Mol Biol. 2017; 1660:143-152.

[32] Mears R, Craven RA, Hanrahan S, Totty N, Upton C, Young SL, Patel P, Selby PJ, Banks RE. Proteomic analysis of melanoma-derived exosomes by two-dimensional polyacrylamide gel electrophoresis and mass spectrometry. Proteomics. 2004; 4(12):1019-4031.

[33] Bandu R, Oh JW, Kim KP. Mass spectrometry-based proteome profiling of extracellular vesicles and their roles in cancer biology. Exp Mol Med. 2019;51(3):1-10.

[34] Everaert C, Helsmoortel H, Decock A, Hulstaert E, Van Paemel R, Verniers K, Nuytens J, et al. Performance assessment of total RNA sequencing of human biofluids and extracellular vesicles. Sci Rep. 2019; 9(1):17574.

[35] Tatischeff I, Larguet E, Falcon-Perez JM, Turpin PY, Kruglik SG. Fast characterization of cell-derived EVs by NTA, cryo-EM, and Raman tweezers microscopy. J Extracell Vesicles. 2012; 1:10.

[36] Mastoridis S, Bertolina GM, Whitehouse G, Dazzi F, Sanchez-Fueyo A, Martinez-Llordella M. Multiparametric analysis of circulating exosomes and other small extracellular vesicles by advanced imaging flow cytometry. Front Immunol. 2018;9:1583.

[37] Sun Y, You S, Tu H, Spillman DR Jr, Chaney EJ, Marjanovic M, Li J, Barkalifa R, Wang J, Hingman AM, Luckey NN, Cradock KA, Liu ZG, Boppart SA. Intraoperative visualization of the tumor microenvironment and quantification of extracellular vesicles by label-free nonlinear imaging. Sci Adv. 2018; 4(12):eaau5603.

[38] Sun Y, Chen E, Thomas J, Liu Y, Tu H, Boppart SA. K-means clustering of coherent Raman spectra from extracellular vesicles visualized by label-free multiphoton imaging. Opt Letters. 2020;45(13):3613-3616.

[39] You S, Tu H, Chaney EJ, Sun Y, Zhao Y, Bower AJ, Liu YZ, Marjanovic M, Sinha S, Pu Y, Boppart SA. Intravital imaging by simultaneous label-free autofluorescence-multiharmonic microscopy. Nat Commun. 2018; 9:2125.

[40] Blacker TS, Mann ZF, Gale JE, Ziegler M, Bain AJ, Szabadkai G, Duchen MR. Separating NADH and NADPH fluorescence in live cells and tissues using FLIM. Nat Commun. 2014; 5:3936.

[41] Liu Z, Pouli D, Alonzo CA, Varone A, Karaliota S, Quinn KP, Munger K, et al. Mapping metabolic changes by noninvasive multiparametic, high-resolution imaging using endogenous contrast. Sci Adv. 2018; 4(3).

[42] Skala MC, Riching KM, Gendron-Fitzpatrick A, Eickhoff J, Eliceiri KW, White JG, Ramanujam N. *In vivo* multiphoton microscopy of NADH and FAD redox states, fluorescence lifetimes, and cellular morphology in precancerous epithelia. Proc Natl Acad Sci. 2007; 104(49):19494-19499.

[43] Chen Y, Periasamy A. Characterization of two-photon excitation fluorescence lifetime imaging microscopy for protein localization. Microscopy Research and Technique. 2003; 63(1).

[44] Berezin MY, Achilefu S. Fluorescence lifetime measurements and biological imaging. Chem Rev. 2010;110(5):2641-2684.

[45] Boyd, R. *Nonlinear Optics*. San Diego, CA: Academic Press, 2003.

[46] Sorrells JE, Martin EM, Aksamitiene E, Mukherjee P, Alex A, Marjanovic M, Boppart SA. Label-free single extracellular vesicle characterization using two-photon fluorescence lifetime imaging microscopy of NAD(P)H. *Submitted*, 2020.

[47] Lakowicz JR, Szmacinski H, Nowaczyk K, Johnson ML. Fluorescence lifetime imaging of free and protein-bound NADH. Proc Natl Acad Sci. 1992;89(4):1271-1275.

[48] Liao, S-C, Sun Y, Coskun Y. FLIM analysis using the phasor plots. ISS Technical Note. 2014.

[49] Schaefer PM, Kalinina S, Rueck A, von Arnim CAF, von Einem B. NADH autofluorescence – a marker on its way to boost bioenergetic research. Cytometry Part A. 2018; 95(1):34-46.

[50] Blacker TS, Duchen MR. Investigating mitochondrial redox state using NADH and NADPH autofluorescence. Free Radic Biol Med. 2016; 100:53-65.

[51] Ostrander JH, McMahon CM, Lem S, Millon SR, Brown JQ, Seewaldt VL, Ramanujam N. Optical redox ratio differentiates breast cancer cell lines based on estrogen receptor status. Cancer Res. 2010;70(11):4759-4766.

[52] Ma N, Digman MA, Malacrida L, Gratton E. Measurement of absolute concentration of NADH in cells using the phasor FLIM method. Biomed Opt Express. 2016; 7(7):2441-2452.

[53] Bower AJ, Sorrells JE, Li J, Marjanovic M, Barkalifa R, Boppart SA. Tracking metabolic dynamics of apoptosis with high-speed two-photon fluorescence lifetime imaging microscopy. Biomed Opt Express. 2019; 10(12): 6408-6421.

[54] Bower AJ, Li J, Chaney EJ, Marjanovic M, Spillman DR, Boppart SA. High-speed imaging of transient metabolic dynamics using two-photon fluorescence lifetime imaging microscopy. Optica. 2018; 5(10):1290-1296.

[55] Lee JH, Rico-Jimenez JJ, Zhang C, Alex A, Chaney EJ, Barkalifa R, Spillman DR, Marjanovic M, Arp Z, Hood SR, Boppart SA. Simultaneous label-free autofluorescence and multi-harmonic imaging reveals *in vivo* structural and metabolic changes in murine skin. Biomed Opt Express. 2019; 10(10):5431-5444.

[56] Shen B, Yan J, Wang S, Zhou F, Zhao Y, Hu R, Qu J, Liu L. Label-free whole-colony imaging and metabolic analysis of metastatic pancreatic cancer by an autoregulating flexible optical system. Theranostics. 2020; 10(4):1849-1860.

[57] Wang M, Tang F, Pan X, Yao L, Wang X, Jing Y, Ma J, Wang G, Mi L. Rapid diagnosis and intraoperative margin assessment of human lung cancer with fluorescence lifetime imaging microscopy. BBA Clinical. 2017; 8:7-13.

[58] Sharick JT, Favreau PF, Gillette AA, Sdao SM, Merrins MJ, Skala MC. Protein-bound NAD(P)H lifetime is sensitive to multiple fates of glucose carbon. Sci Rep. 2018; 8:5456.

[59] The Human Protein Atlas, Version 19.3; https://www.proteinatlas.org/, accessed June 2020.

[60] Ettelaie C, Collier ME, Maraveyas A, Ettelaie R. Characterization of physical properties of tissue factor-containing microvesicles and a comparison of ultracentrifuge-based recovery procedures. J Extracell Vesicles. 2014; 3.

[61] Bodega G, Alique M, Bohorquez L, Moran M, Magro L, Puebla L, Ciordia S, Mena MC, Arza E, Ramirez MR. Young and especially senescent endothelial microvesicles produce NADPH: the fuel for their antioxidant machinery. Ox Med Cell Longev. 2018; 2018:3183794.

[62] Lindeberg T. Detecting salient blob-like image structures and their scales with a scale-space primal sketch: a method for focus-of-attention. Int J Comput Vis. 1993; 11(3):283-318.

[63] Khoo BL, Grenci G, Lim YB, Lee SC, Han J, Lim CT. Expansion of patient-derived circulating tumor cells from liquid biopsies using a CTC microfluidic culture device. Nat Protoc. 2018;13(1):34-58.

[64] Gholizadeg S, Draz MS, Zarghooni M, Sanati-Nezhad A, Ghavami S, Shafiee H, Akbari M. Microfluidic approaches for islation, detection, and characterization of extracellular vesicles: current status and future directions. Biosensors and Bioelectronics. 2017; 91(15):588-605.

[65] Jeyaram A, Jay SM. Preservation and storage stability of extracellular vesicles for therapeutic applications. AAPS J. 2019; 20(1):1.

[66] Lorincz AM, Timar CI, Marosvari KA, Veres DS, Otrokocsi L, Kittel A, Ligeti E. Effect of storage on physical and functional properties of extracellular vesicles derived from neutrophilic granulocytes. J Extracell Vesicles. 2014; 3:25465.

[67] Oliveira DL, Freire-de-Lim CG, Nosanchuk JD, Casadevall A, Rodrigues ML, Nimrichter L. Extracellular vesicles from cryptococcus neoformans modulate macrophage functions. Infect Immun. 2010;78(4):1601-1609.

[68] van der Vos KE, Abels ER, Zhang X, Lai C, Carrizosa E, Oakley D, Prabhakar S, et al. Directly visualized glioblastoma-derived extracellular vesicles transfer RNA to microglia/macrophages in the brain. Neuro-Oncology. 2016;18(1):58-69.

[69] Alfonso-Garcia A, Smith TD, Datta R, Luu TU, Gratton E, Potma EO, Lie WF. Label-free identification of macrophage phenotype by fluorescence lifetime imaging microscopy. 2016;21(4):046005.

[70] Kanada M, Bachmann MH, Contag CH. Signaling by extracellular vesicles advances cancer hallmarks. Trends Cancer. 2016;2(2):84-94.

[71] Zomer A, Maynard C, Verwij F, Kamermans A, Schafer R, Beerrling E, Schiffelers RM, de Wit E, Berenguer J, Ellenbroek SIJ, Wurdinger T, Pegtel DM, van Rheenen J. *In Vivo* imaging reveals extracellular vesicle-mediated phenocopying of metastatic behavior. Cell. 2015; 161(5):1046-1057.

[72] Taylor J, Azimi I, Monteith G, Bebawy M. Ca2+ mediates extracellular vesicle biogenesis through alternate pathways in malignancy. J Extracell Vesicles. 2020; 9(1):1734326.

[73] Chen WW, Balaj L, Liao LM, Samuels ML, Kotsopoulos SK, Maguire CA, et al. BEAMing and droplet digital PCR analysis of mutant IDH1 mRNA in glioma patient serum and cerebrospinal fluid extracellular vesicles. Mol Ther Nucleic Acids. 2013; 2(7): e109.

[74] Green TM, Alpaugh ML, Barsky SH, Rappa G, Lorico A. Breast cancer-derived extracellular vesicles: characterization and contribution to the metastatic phenotype. Biomed Res Int. 2015; 2015:634865.

[75] Choi D, Go G, Kim DK, Lee J, Park SM, Di Vizio D, Gho YS. Quantitative proteomic analysis of trypsin-treated extracellular vesicles to identify the real-vesicular proteins. J Extracell Vesicles. 2020;9(1):1757209.

[76] Vesiclepedia.com

[79] Melo, SA, Luecke LB, Kahlert C, Fernandez AF, Gammon ST, Kaye J, et al. Glypican1 identifies cancer exosomes and facilitates early detection of cancer. Nature. 2015; 523(7559): 177-182.

[78] Wang S, Kojima K, Mobley JA, West AB. Proteomic analysis of urinary extracellular vesicles reveal biomarkers for neurologic disease. EBioMedicine. 2019; 45: 351-361.

[77] Guha D, Lorenz DR, Misra V, Chettimada S, Morgello S, Gabuzda D. Proteomic analysis of cerebrospinal fluid extracellular vesicles reveals synaptic injury, inflammation, and stress response markers in HIV patients with cognitive impairment. J Neuroinflammation. 2019; 16: 254.

[80] Conde-Vancells J, Rodriguez-Suarez E, Embade N, Gil D, Matthiesen R, Valle M, Elortza F, Lu SC, Mato JM, Falcon-Perez JM. Characterization and comprehensive proteome profiling of exosomes secreted by hepatocytes. J Proteome Res. 2008; 7(12): 5157-5166.

[81] Fevrier B, Vilette D, Archer F, Loew D, Faigle W, Vidal M, L Hubert, Raposo G. Cells release prions in association with exosomes. Proc Natl Acad Sci. 2004; 101(26):9683-9688.

[82] Hegmans JP, Bard MP, Hemmes A, Luider TM, Kleijmeer MJ, Prins JB, Zitvogel L, Burgers SA, Hoogsteden HC, Lambrecht BN. Proteomic analysis of exosomes secreted by human mesothelioma cells. Am J Pathol. 2004; 164(5):1807-1815.

[83] Zumaquero E, Munoz P, Cobo M, Lucena G, Pavon EJ, Martin A. Exosomes from human lymphoblastoid B cells express enzymatically active CD38 that is associated with signaling complexes CD81, Hsc-70, and Lyn. Exp Cell Res. 2010; 316(16):2692-2706.

[84] Morandi F, Marinpietri D, Horenstein AL, Bolzoni M, Toscani D, Costa F, et al. Microvesicles released from multiple myeloma cells are equipped with ectoenzymes belonging to canonical and non-canonical

adenosinergic pathways and produce adenosine from ATP and NAD+. Oncoimmunology. 2018; 7(8): e1458809.

[85] Bodega G, Alique M, Puebla L, Carracedo J, Ramirez RM. Microvesicles: ROS scavengers and ROS producers. J Extracell Vesicles. 2019; 8(1): 1626654.

[86] Verdin E. NAD+ in aging, metabolism, and neurodegeneration. Science. 2015; 350(6265):1208-1213.

[87] Debarre D, Supatto W, Beaurepaire E. Structure sensitivity in third-harmonic generation microscopy. Opt Letters. 2005; 30(16):2134-2136.

[88] Tu H, Liu Y, Turchinovich D, Marjanovic M, Lyngso J, Laegsgaard J, Chaney EJ, Zhao Y, You S, Wilson WL, Xu B, Dantus M, Boppart SA. Stain-free histopathology by programmable supercontinuum pulses. Nat Photonics. 2016; 10(8):534-540.